a patient body from the start of proton beam irradiation to 200 s after the end of irradiation using BOLPs-RGp. Up to now, the number of cases measured is about 150, such as cases involving head and neck, prostate, liver, lung, and brain. Furthermore, an apparatus for viewing and analysis, which exclusively uses the data measured by BOLPs-RGp, has been developed and used.[2] Study involving analysis of irradiated body tissues of patients using clinical data has been reported,[1,2] which proved that the use of BOLPs-RGp in clinical proton therapy is very useful for quality assurance and control and provides improvement in terms of accuracy.

Research in the monitoring of the proton-irradiated volume via nucleus activation has been worked on.[1–17] To verify the absolute accuracy of planned dose distributions using measured activity distributions, we have to simulate activity distributions from dose distributions. Research on the simulation of activity distributions has been carried out. One of the methods is calculation of activity distributions using a Monte Carlo simulation, in which data of cross sections for the rate of target nuclear fragment reactions between proton and nuclei compositing patients' bodies are used with GEANT4 and FLUKA.[18–20] And, in carbon ion therapy it is reported that a technique of activity simulation utilizes the database of Monte Carlo calculated activity distribution which is formed in ^{12}C pencil beam irradiation of PMMA targets.[21] That research group deals with both projectile and target nuclear fragmentation reactions but only target nuclear fragments are treated in this study. It is difficult to determine the value of cross sections as the value is dependent on proton energy and the species of positron emitter nuclei that are generated. At present, the reported data of cross sections are not sufficient for simulation of activity distributions in terms of quantity and accuracy.[22] However, determination of the value of cross sections is now underway in other groups, and it may be expected that data of cross sections that are sufficient for simulation will be obtained. Therefore, it can be said that the calculation accuracy of simulation based on a detailed physics process using a Monte Carlo simulation will likely improve with a corresponding increased accuracy in the knowledge of reaction cross sections in the near future.

To use the simulation in clinical therapy, the calculation time is one of the necessary conditions in addition to the calculation accuracy. Because an enormous amount of data is essential for calculation using the Monte Carlo simulation, which is a statistical calculation method with random numbers, it takes hours to obtain the result of calculation. Although there are methods, like lookup table, e.g., phase-space file, to improve the speed of simulation such as GEANT and FLUKA, it may be difficult to adopt the simulation system using the Monte Carlo simulation for an on-site location near a clinical therapy where it is now needed for treatment of a lot of patients. However, since BOLPs-RGp is now used in clinical therapy, there are ongoing efforts of constructing a simulation system that meets the requirements in terms of both accuracy and calculation time for clinical use. It is necessary to develop a new calculation algorithm that can be used in clinical therapy to provide improvements in proton therapy using BOLPs-RGp.

The purpose of this study is to develop a new calculation algorithm for the simulation system of imaging of activity distributions corresponding to the planned irradiation volume in clinical proton therapy.

II. MATERIAL AND METHOD

II.A. The new calculation algorithm of activity distributions proposed in this study

The necessary conditions of the calculation algorithm of activity distributions are high speed and high accuracy in calculation for utilization of the simulation system for imaging of activity distributions in clinical proton therapy. The new algorithm was developed using activity pencil beam kernel for calculation of activity distributions in this study. The data of measured depth activity distributions and calculated lateral activity distributions are used for obtaining the activity pencil beam data.

II.A.1. Depth activity distribution

A quantity of positron emitter nuclei generated from target nuclear fragment reactions is affected by each value of the cross section for the reactions within the range of energy used for proton therapy. Since the accuracy of the value regarding the cross section has a direct effect on the accuracy of the simulation, the determined value for the cross section is very important in the simulation of activity distributions. However, it cannot be said that the data of the cross section required for simulation calculation are sufficient in terms of accuracy and quantity at present. The phantom study using PET/CT imaging suggested the potential of millimeter accuracy in proton therapy.[16] But in patient study, it was reported that the accuracy of a simulation that calculated activity distributions in a patient body was within 30% by uncertainties of cross section, washout effects, and stoichiometric composition in patient body.[15]

Therefore, improvements in the accuracy of values regarding the cross sections of target nuclear fragment reactions are needed to use the simulation of activity distributions to image the planned and proton-irradiated volume with high accuracy in clinical proton therapy. In this study, "virtual positron emitter nuclei ($^{12}C_{virtual}$,$^{16}O_{virtual}$, and $^{40}Ca_{virtual}$)" was defined as the nuclei merged of various positron emitter nuclei generated from each target nucleus by target nuclear fragment reactions with irradiated proton beam (see Eq. (1)).

$$\begin{aligned} &^{12}C(p,x)^{11}C,^{10}C,\text{etc.} \rightarrow {}^{12}C(p,x)^{12}C_{virtual},\\ &^{16}O(p,x)^{15}O,^{14}O,\text{etc.} \rightarrow {}^{16}O(p,x)^{16}O_{virtual},\\ &^{40}Ca(p,x)^{39}Ca,^{38}Ca,\text{etc.} \rightarrow {}^{40}Ca(p,x)^{40}Ca_{virtual}. \end{aligned} \quad (1)$$

A new approach was adopted that uses measured activity distributions of virtual positron emitter nuclei when the proton beam irradiates a compound containing target nuclei, not which uses values of reaction cross section determined one by one for each reaction channel. The data of measured activity distributions of virtual positron emitter nuclei that we obtained

in this study cover the information of the most relevant reaction channels generating positron emitter nuclei in irradiation targets. Moreover, decrease of energy and attenuation of incident proton flux occur at the depth point in thick targets. A similar attenuate phenomenon occurs in a patient body irradiated by proton beam. Therefore, the data are significant for this study in view of future application to describe the nuclear fragmentation reactions occurring in the human body. In the calculation of activity distributions, measured data of depth activity distributions can improve the accuracy of calculation.

II.A.2. Calculation algorithm of activity distributions for simulation of imaging of planned irradiation volume by proton beam: activity pencil beam algorithm (APB algorithm)

The accuracy of calculation using the Monte Carlo simulation is affected by statistical error, which depends on the total number of histories. Calculation must be performed with a sufficiently large number of histories to meet the accuracy required in each case. With the Monte Carlo simulation, it takes hours to obtain the result of calculation with the accuracy required for clinical use. A simulation with calculation time within several minutes is demanded for proton therapy of many patients in hospital.

For simulation system of imaging of activity distributions in daily proton therapy, the activity pencil beam algorithm (APB algorithm) was developed as a new calculation algorithm with both accuracy and high speed. The pencil beam algorithm is a standard algorithm of dose calculation in proton therapy. This algorithm is a technique for calculation that considers depth dose distributions along the direction that the proton beam travels, and that also approximates lateral dose distributions of the Gaussian form at every depth point by effect of multiple Coulomb scattering. However, effect of the scattering by inhomogeneous density in material from axis of beam direction is not considered in the pencil beam algorithm. Therefore, the accuracy of calculation of dose distributions deteriorates in areas of a steep density gradient, such as lungs, bone, and nasal cavity. Although the accuracy of calculation using pencil beam algorithm may deteriorate in a site of a patient's body, the algorithm is generally used for dose calculation in clinical proton therapy because it is well balanced between accuracy and calculation time required in clinical use. These considerations are similar in APB algorithm for the calculation of activity distributions formed by target nuclear fragment reactions between proton and nuclei compositing a human body.

In APB algorithm, depth and lateral activity distributions are defined by measurement of activity of $^{12}C_{virtual}$, $^{16}O_{virtual}$ and $^{40}Ca_{virtual}$ nuclei and calculation of multiple Coulomb scattering. The activity pencil beam kernel, $A_{mono}(X_{virtual}; r, z, t_{ag})$, is shown in Eq. (2) as following:

$$A_{mono}(X_{virtual}; r, z, t_{ag}) = A_{meas.}(X_{vitrual}; z, t_{ag}) \cdot \frac{1}{2 \cdot \pi \cdot \sigma_r(z)^2} \cdot \exp\left(-\frac{r^2}{2 \cdot \sigma_r(z)^2}\right),$$
$$\{X_{vitrual} = {}^{12}C_{vitrual}, {}^{16}O_{vitrual}, {}^{40}Ca_{vitrual}\}. \quad (2)$$

Here, $A_{meas.}(X_{virtual}; r, z, t_{ag})$ is measured depth activity distribution, $X_{virtual}$ virtual positron emitter nuclei, r lateral position from axis of beam direction, z depth point in water equivalent material, t_{ag} time after generated virtual positron emitter nuclei, and σ_r the parameter of lateral distribution decided by effect of multiple Coulomb scattering. There are various techniques to decide parameter of σ_r.[23–26] If APB algorithm is adopted, it can be estimated that the calculation time will be several minutes because activity calculation time is similar to dose calculation time using pencil beam algorithm theoretically. Therefore, the calculation time required in clinical use will be satisfied.

II.B. Beam ON-LINE PET system mounted on a rotating gantry port: BOLPs-RGp

The beam ON-LINE PET system mounted on a rotating gantry port (BOLPs-RGp) installed on the proton beam line in our treatment room in the National Cancer Center, Kashiwa, was developed for proton beam monitoring and is used in clinical proton therapy.[1] The opposing detector heads of planar type with a high position resolution were composed of BGO crystals with a crystal size of $2 \times 2 \times 20$ mm^3. The field of view (FOV) at the iso-center was 164.8×167.0 mm^2. The center of its detection area corresponded with the iso-center under a condition where the detectors were opposite each other on a rotating gantry port. The opposing detectors rotated together with the rotating gantry. The detector heads opposite each other were installed along the axis of the proton beam direction and an area in the range direction of the proton beam can be observed. A PET image is reconstructed using a maximum likelihood algorithm taking into consideration the attenuation coefficient of 511-keV gamma rays in the patient's body calculated using the patient's planning CT image data. The distance between the opposing detector heads can be adjusted from 30 to 100 cm.

With regard to the performance of this detection system, the maximum collection rate of the data for the coincident detection was about 1 Mcps. The position resolution of measuring activity was about 2 mm of the full width at half maximum (FWHM) at the iso-center in the FOV in an experiment using a ^{22}Na point source. The detection efficiency was calibrated using a thin-flat acrylic container filled with ^{18}F solution at each distance between detector heads from 30 to 100 cm. In addition, the viewer of activity for clinical analysis (VACA; TR Japan), which is a display and analysis tool for the data detected by BOLPs-RGp, was developed and used.[2]

II.C. Measurement of depth activity distributions

II.C.1. Irradiation target for measurements of activity

The main nuclei of which human body tissue is composed and which cause target nuclear fragment reactions with proton are the following: ^{12}C, ^{14}N, ^{16}O and ^{40}Ca, in the range of proton beam energy used in proton therapy (i.e., 0–250 MeV). Important nuclei for imaging of irradiated volume in a patient's body are ^{12}C, ^{16}O, and ^{40}Ca nuclei by the ratio of

the four nuclei in a human body tissue and the data of a reaction cross section for target nuclear fragment reactions in the range of proton beam energy used in proton therapy.[2] Therefore, ^{12}C nuclei and ^{16}O nuclei, as well as ^{40}Ca nuclei, were selected as the target nuclei, and activity distributions of virtual positron emitter nuclear formed from a reaction between proton and the target nuclei were obtained.

Polyethylene (PE: CH_2) and water were the irradiated targets, and activity distributions that originated from a reaction between proton and ^{12}C nuclei or ^{16}O nuclei were measured. In the experiment using the two targets of PE and water, hydrogen nuclei have no part in the target nuclear fragment reactions. Consequently, the results of measurement for the two targets are equal to the results of reaction for ^{12}C nuclei and ^{16}O nuclei with proton. The target of PE was made of polyethylene with a high density of 0.96 g/cm^3. By addition of a little gelatin (the mass of the gelatin was 1.95% the mass of water) to pure water, a target of water with no flow was made. Because handling of solid calcium is difficult, packed powder of calcium oxide (CaO), which can be handled comparatively easily in a container made of PE, was the target of ^{40}Ca nuclei. The results of measurement of CaO target included the reaction of proton and ^{40}Ca nuclei as well as ^{16}O nuclei. Then, results of only the reaction of ^{40}Ca nuclei and proton were obtained by subtracting the results of reaction of ^{16}O nuclei and proton from the results of CaO target. The difference of proton fluence calculated in CaO target and water target was about 5% around range point of 223 MeV proton beam. Result of activity distribution of $^{40}Ca_{virtual}$ nuclei was considered by the difference of proton flux attenuation in CaO and water targets.

Considering the detecting area of BOLPs-RGp and the size of the proton beam, the size of PE target was $8 \times 8 \times 12$ cm^3. Targets of water and CaO were the containers made of PE with a thickness of 5 mm, filled with the water including a little gelatin or the powdered CaO, and the inside volume of the containers was $8 \times 8 \times 12$ cm^3 (see Fig. 1). To acquire the depth activity distributions produced by ^{40}Ca nuclei and proton nuclei, the number of irradiated proton to target was normalized using activity value of 5-mm thickness wall on the side of the beam entrance in container of PE for water (H_2O) and CaO targets. In experiment of range measurement after passing through the target by the proton beam, the water equivalent length of 1 cm PE and CaO were 1.02 cm and 1.15 cm, respectively.

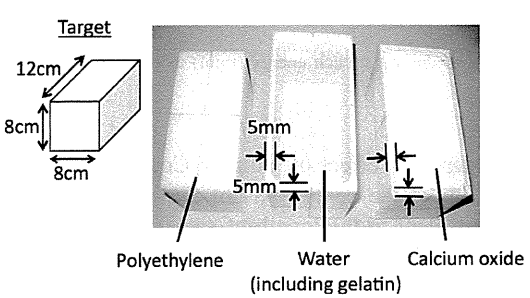

FIG. 1. Targets consisted of the target nuclei, that is, ^{12}C, ^{16}O, and ^{40}Ca. The left is polyethylene, the middle is water including gelatin, and the right is calcium oxide.

II.C.2. Proton beam irradiations to target

Each target was irradiated using mono-energetic proton beams with energies of 223, 179, and 138 MeV. The irradiated dose was equivalent to 15 Gy at around the Bragg Peak to reduce the statistical error of measurement activity of virtual positron emitter nuclei in irradiation target. The proton beam of 2 cm in diameter at the iso-center was irradiated in 2–20 s. Each target was measured on the condition that intensity of proton beams in each measurement and irradiation time in the same energy was constant.

$^{40}Ca_{virtual}$ nuclei include positron emitter nuclei with short half-lives around 1 s, such as ^{38}Ca nuclei and ^{39}Ca nuclei. Therefore, an additional measurement such that the time of proton beam irradiated to CaO target was less than 1 s was done. The activity measurement was performed twice for each proton beam energy in order to measure the generated positron emitter nuclei of short half-lives with improved statistics.

II.C.3. Measurement of depth activity distributions using BOLPs-RGp

The depth activity distribution of virtual positron emitter nuclei generated by proton beam irradiation in a target was measured using BOLPs-RGp. The irradiation target was set up at the position where the center of the target corresponded to the iso-center (see left side of Fig. 2). The distance between the opposing detector heads of PET was 90 cm and the gantry angle was 270°. The measurement time was 303.3 min (5 h 3 min and 20 s) in one irradiation for each target for obtaining enough characteristic of virtual positron emitter nuclei generated by proton beam irradiation. The output of measurement values occurred every second from the start of measurement to 200 s and, after 200 s, an integrated count for every 10 s was output. For the CaO target, an additional measurement of 200 s was performed. The output of measurement values occurred every second for measurement of virtual positron emitter nuclei with short half-lives generated by proton irradiation.

The FOV of BOLPs-RGp was about 16 cm; however, the proton beam range in water was about 14–30 cm at 138–223 MeV. The area was so small that measurement could not be finished in a single session. Therefore, the whole measurement area of the target was divided in the depth direction, and each separate measurement area was measured gradually. The measurement area was shown in right side of Fig. 2. The numbers of separate areas were five at 223 MeV, three at 179 MeV, and two at 138 MeV. The depicted proton dose distributions were measured using water phantom. The depth of the dose distribution shows water equivalent length (WEL). The method of gradual measurement involved the measurement area being moved by changing the thickness of a fine degrader, which adjusted the beam range, and inserting the PE material with homogeneous thickness into the place at which the patient's bolus was put. Measured depth activity

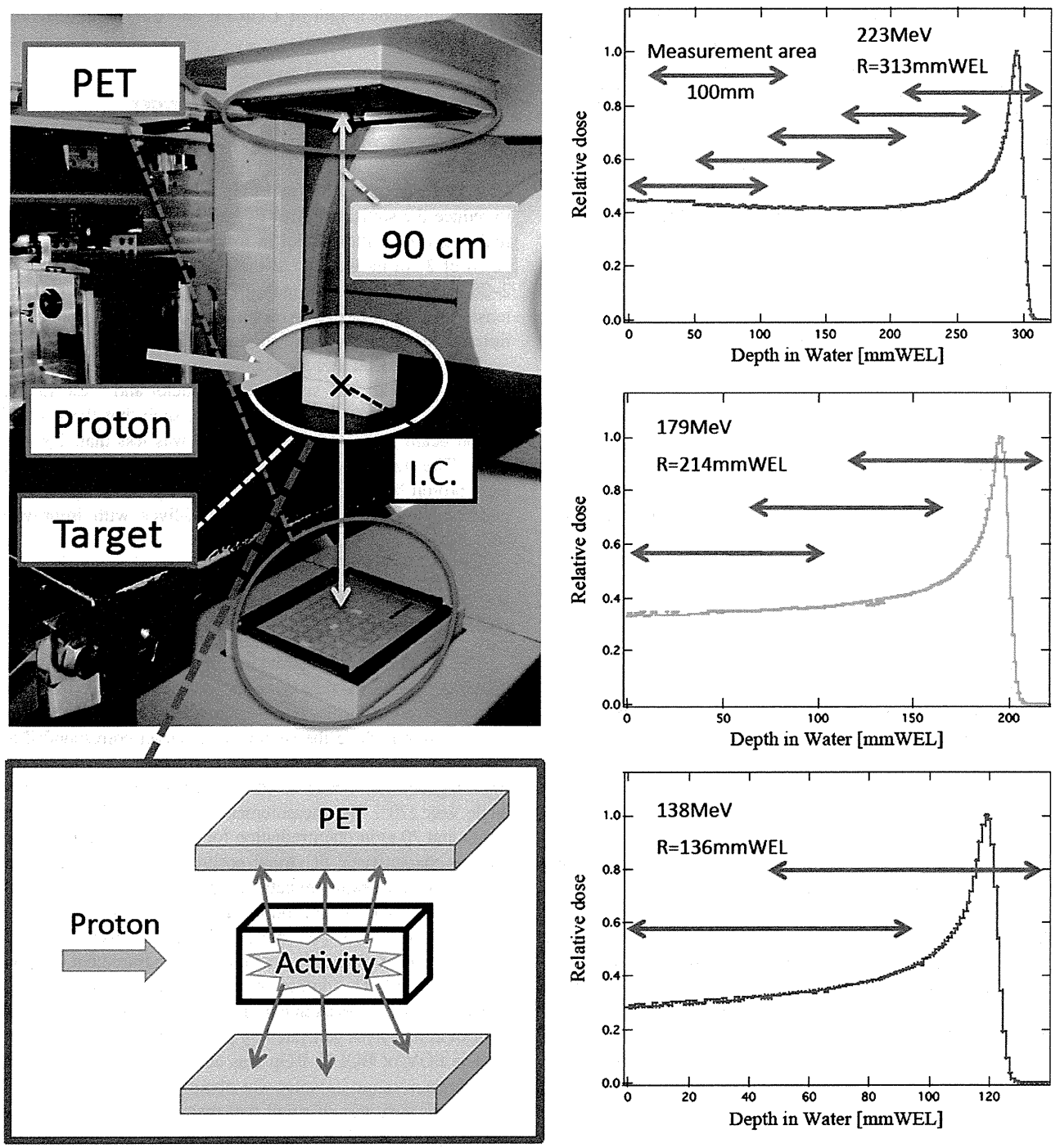

FIG. 2. The design of a system to measure activity distributions (left) and measurement area of the target each energy (right) using BOLPs-RGp in NCC, Kashiwa.

distributions for every energy and target were acquired by connecting each measured activity distribution gradually.

II.D. Making of activity pencil beam kernel using the measured activity distributions

The pencil beam algorithm takes into consideration both depth activity distributions along the direction toward the center axis of proton beam travel and lateral activity distribution at depth by effect of multiple Coulomb scattering. In the direction of the center axis of the proton beam, water length equivalent to the length of each calculation grid was calculated, and this calculated length was given a one-dimensional value of percent depth activity (PDA). The effect of multiple Coulomb scattering was included to lateral activity distribution with Gaussian form similarly to proton dose calculation by pencil beam algorithm. The formula

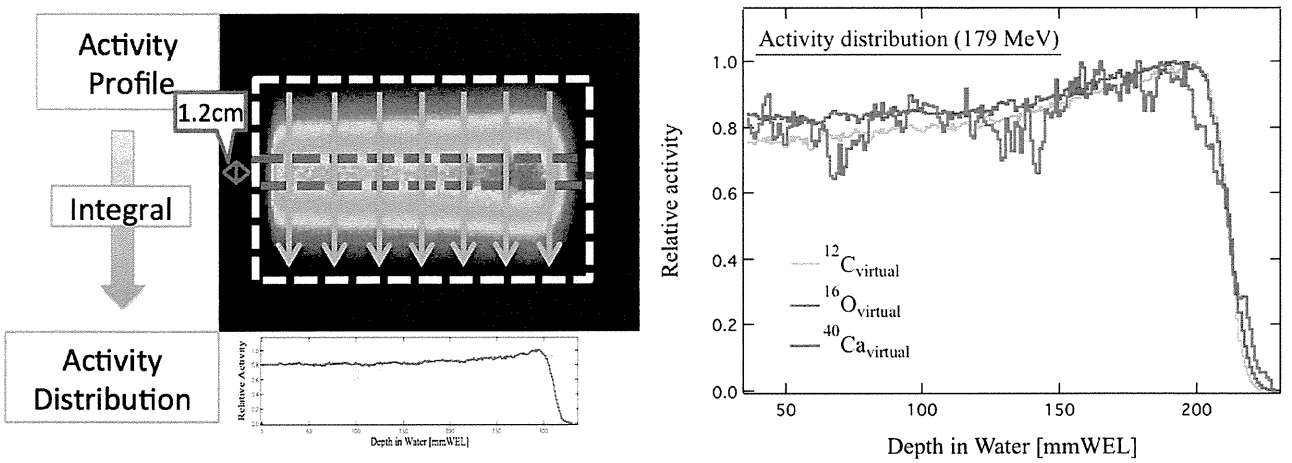

FIG. 3. The approach for making activity distributions from integrated measured two-dimensional activity profile (left). The measured depth activity distributions of virtual positron emitter nuclei that were obtained by irradiating proton beam of 179 MeV to every target nucleus (right).

proposed by Lynch was used for the activity pencil beam kernel in this study.[25]

III. RESULTS AND DISCUSSION

III.A. Results of measured depth activity distributions

The profile of a target activity obtained using BOLPs-RGp is two-dimensional information, which is taken in two perpendicular directions to the opposing detectors of PET installed on BOLPs-RGp. As shown to the left of Fig. 3, first, the measured two-dimensional activity profile was integrated in the direction perpendicular to the beam axis. Second, divided measured data were revised, such as by normalizing the number of incident proton, and the revised data were gathered and connected. This was the case for the results of measured depth activity distributions for every energy and target. Figure 3 shows the measured depth activity distributions obtained by irradiating proton beam of 179 MeV for every target nucleus. In terms of the distribution of $^{40}Ca_{virtual}$ nuclei, it can be seen that the dispersion of $^{40}Ca_{virtual}$ nuclei distribution is greater than that of the other two nuclei. This can be explained by there being statistical dispersion in $^{40}Ca_{virtual}$ nuclei data because $^{40}Ca_{virtual}$ nuclei data are obtained by subtracting $^{16}O_{virtual}$ nuclei data from the CaO data. The dispersion could be reduced by increasing the measurement time and the number of measurement data.

III.B. Verification of the form and the time dependence of depth activity distributions

III.B.1. Depth activity distributions by starting time of measurement after proton beam irradiation

Activity distribution is based on the information of virtual positron emitter nuclei generated by target nuclear fragment reactions. The quantity of activity detected by BOLPs-RGp is dependent on the time of irradiation and detection because positron emitter nuclei have half-lives that differ for every kind of nucleus. Therefore, it is necessary to verify the time dependence of the form of a measured activity distribution during the measurement period. The irradiation time of a proton beam varies for each patient and treatment by the difference of fractional dose or whether irradiation with synchronized respiration was carried out. Change of depth activity distribution by period of proton irradiation was verified and estimated by the measured activity data using BOLPs-RGp in clinical treatment.[1,2]

About five areas of depth activity distributions of $^{12}C_{virtual}$ nuclei obtained using a proton beam of 223 MeV irradiating PE targets were verified. Figure 4 is measurement results of depth activity distributions by starting time of measurement after 223 MeV proton beam irradiation to PE target. Two activity distributions ((a) and (b)) shown in the figure are measured in the area around entrance of PE target with incident proton beam and the proton beam range of 223 MeV. The measured depth activity distribution data of 100 s was analyzed by the time from irradiation to starting BOLPs-RGp measurement, *Ts*, of 0 (immediately after the irradiation), 0.5, 1, 2, 3, 5, 7, and 10 min. In the area around entrance of PE target with incident proton beam of 223 MeV, the change of the form of depth activity distributions to the change of *Ts* was within ±10% [Fig. 4(a)]. In the deepest area around the beam range, although the forms of six depth activity distributions with *Ts* greater than 1 min were similar, the forms of distributions about *Ts* = and 0.5 were greatly different from others [Fig. 4(b)]. In these circumstances, it was clear that the form of depth activity distributions changed with the depth and the irradiation time.

Depth activity distributions of $^{12}C_{virtual}$ nuclei obtained by proton beam irradiation to PE are the function of the time and the depth, which were expressed by two elements: ^{10}C nucleus whose half-life is about 20 s and ^{11}C nucleus whose half-life is about 20 min. ^{10}C nuclei with a short half-life are included in activity data measured immediately after proton beam irradiation. As time passed, a difference in the form of the depth activity distribution occurred because mainly information on ^{11}C nuclei became available. Therefore, it can be considered that the reason why the form of the depth activity distribution changed is that the ratio of the amount of information about ^{10}C nuclei and ^{11}C nuclei in the measured data changed with time from the end of irradiation to the start of the measurement (i.e., *Ts*).

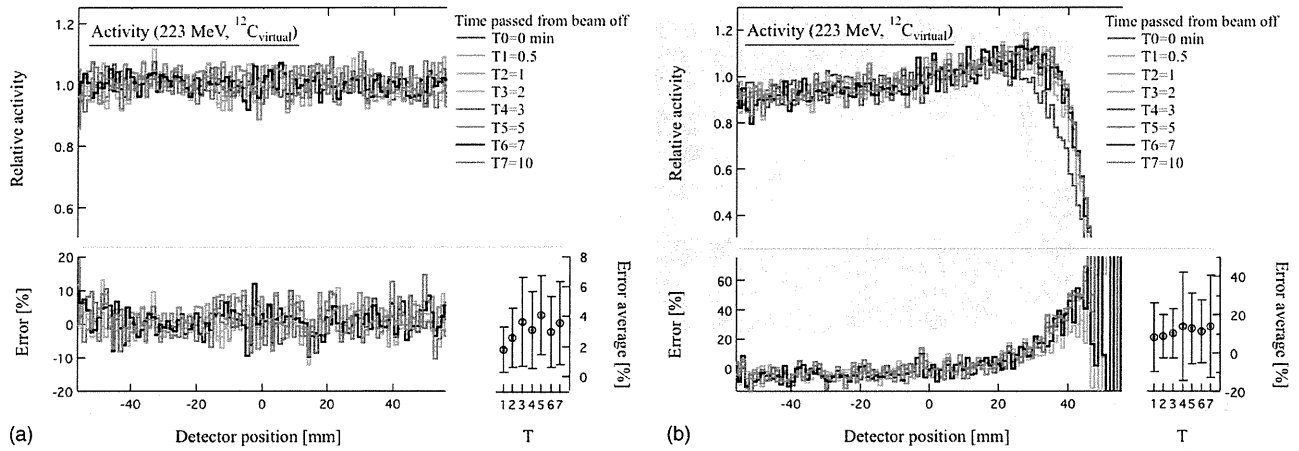

FIG. 4. Depth activity distributions of $^{12}C_{virtual}$ nuclei by starting time of measurement after 223 MeV proton beam irradiation to PE target are shown. (a) The area around entrance of PE target with incident proton beam and (b) the area around the proton beam range of 223 MeV. The lower right-hand graph showed the average error and deviation to data of T0 ($Ts = 0$).

As for the activity distribution around the beam range in Fig. 4(b), it can be observed that the range of the depth activity distribution at $Ts = 0$ is shallower than the other six distributions with Ts greater than 1 min. One neutron is generated by the reaction to generate a ^{11}C nucleus, and two neutrons are generated by the reaction to generate a ^{10}C nucleus in the target fragment reaction between ^{12}C nuclei and proton. The reaction to generate a ^{10}C nucleus needs more proton energy to generate a neutron than the reaction to generate a ^{11}C nucleus. Therefore, it can be considered that the range of depth activity distributions formed mainly from the information of ^{10}C nuclei was shallower than the distributions of the others. Moreover, it was observed that there was hardly a difference in depth activity distributions for Ts greater than 1 min. This may suggest that the quantitative proportion of generated ^{10}C nuclei to $^{12}C_{virtual}$ nuclei was small.

III.B.2. Half-lives of virtual positron emitter nuclei ($^{12}C_{virtual}$, $^{16}O_{virtual}$, and $^{40}Ca_{virtual}$)

It turned out that the simulation of activity distributions had to take the time dependence of the form of depth activity distributions into consideration given the result of Sec. III B 1 above. Therefore, the change of activity-intensity at each depth point with the passage of time was analyzed for the measured activity distributions for every target nucleus. The decay curves of measured activity data during the period of measurement (about 5 h) in a very small volume, which was set up around the depth point in the target, were obtained and the characteristics of the decay curves were identified. 10–16 points for analysis were set up and all targets and energies were analyzed in consideration of the form of the measured activity distribution. Figure 5 shows the result about $^{12}C_{virtual}$ nuclei by irradiation of 223 MeV proton beam.

The virtual positron emitter nuclei generated by proton irradiation were roughly divided into two elements by the length of the nucleus half-life for all the target nuclei in this study. The two kinds of nuclei whose half-lives are 20 min (^{11}C nucleus) and 20 s (^{10}C nucleus) are generated from ^{12}C nuclei as target nuclei, in the same way, 10–20 min (^{11}C and ^{13}N nuclei) and several minutes or under (^{15}O, ^{14}O, and ^{10}C nuclei) are done from ^{16}O nuclei and under 1 s (^{38}Ca and ^{39}Ca nuclei) and several minutes (^{38}K nuclei) are done from ^{40}Ca nuclei. Therefore, the decay curves of measured activity data in small volumes, which were set up for every depth point for analysis using Eq. (3) constructed with elements separated into two groups of half-lives, were approximated.

$$N_{act.}(z,t) = A_{T_{long}}(z) \cdot \left(\frac{1}{2}\right)^{\frac{t}{T_{long}(z)}} + A_{T_{short}}(z) \cdot \left(\frac{1}{2}\right)^{\frac{t}{T_{short}(z)}}. \quad (3)$$

Here, $N_{act.}$ represents measured activity data, t measurement time, T_{long} and T_{short} half-lives, and $A_{T_{long}}$ and $A_{T_{long}}$ total measured activity of each half-life. N_{act} is total measured activity at t = 0. Figure 5 shows the decay curves that were obtained from measured activity data of $^{12}C_{virtual}$ nuclei using 223 MeV proton beam and the fitting curves at 10

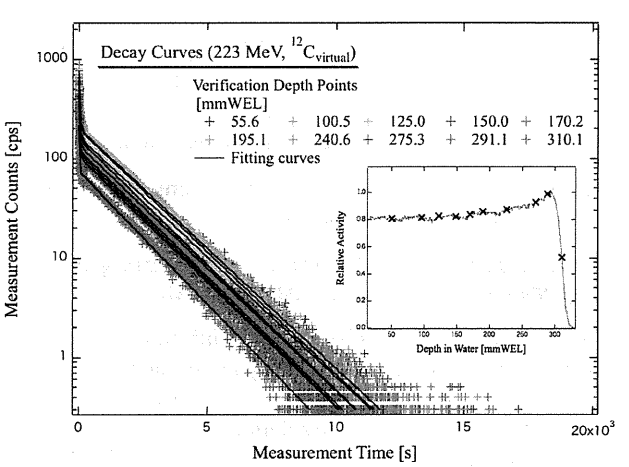

FIG. 5. The decay curves of measured activity data of $^{12}C_{virtual}$ nuclei during the measurement period (about 5 h) and the curves approximated using Eq. (3) in a very small volume at each depth point (223 MeV, PE target).

TABLE I. The results of approximation with two elements for each target and energy to the depth.

Target	Energy [MeV]	$R_{T_{long}}$ ($\pm\Delta R_{T_{long}}$)	T_{long} ($\pm\Delta T_{long}$) [s]	$\Delta R_{T_{long}}/R_{T_{long}}$ [%]	$\Delta T_{long}/T_{long}$ [%]
^{12}C	223	0.274 (±0.030)	1201 (±30)	10.8	2.5
	179	0.313 (±0.073)	1215 (±12)	23.4	1.0
	138	0.337 (±0.085)	1208 (±8)	25.2	0.7
^{16}O	223	0.029 (±0.011)	1354 (±339)	38.4	25.1
	179	0.030 (±0.007)	1257 (±74)	22.4	5.9
	138	0.036 (±0.011)	1078 (±69)	29.6	6.4
^{40}Ca	223	0.003 (±0.001)	582 (±84)	28.7	14.4
	179	0.002 (±0.000)	631 (±57)	24.7	9.1
	138	0.002 (±0.001)	576 (±36)	23.0	6.2
Target	Energy [MeV]	$R_{T_{short}}$ ($\pm\Delta R_{T_{short}}$)	T_{short} ($\pm\Delta T_{short}$) [s]	$\Delta R_{T_{short}}/R_{T_{short}}$ [%]	$\Delta T_{short}/T_{short}$ [%]
^{12}C	223	0.726 (±0.030)	20 (±3)	4.1	14.2
	179	0.687 (±0.073)	20 (±1)	10.7	3.5
	138	0.663 (±0.085)	19 (±1)	12.8	3.3
^{16}O	223	0.971 (±0.011)	139 (±6)	1.2	4.6
	179	0.970 (±0.007)	132 (±2)	0.7	1.5
	138	0.964 (±0.011)	126 (±2)	1.1	1.3
^{40}Ca	223	0.997 (±0.001)	1 (±0)	0.1	13.0
	179	0.998 (±0.000)	1 (±0)	0.0	7.0
	138	0.998 (±0.001)	1 (±0)	0.1	7.1

depth points. Fitting results of decay curves for each target and energy at the depth points were summarized in Table I.

The elements with short half-lives were approximated with higher accuracy than the elements with long half-lives in terms of both half-lives and ratios of these elements in the decay curves obtained from the measured activity data. Probably, the virtual positron emitter nuclei with short half-life had greater influence on the quantity of activity originating from virtual positron emitter nuclei, which might be detected immediately after proton irradiation (that is, $N_{act.}(z, t = 0)$), than the virtual positron emitter nuclei with a long half-life. Table I suggests that the activity distributions obtained immediately after proton irradiation were formed by the activity that originated from virtual positron emitter nuclei with short half-lives mainly for all targets and energies. About 30% of activity distributions of $^{12}C_{virtual}$ nuclei were contributed to by the activity of virtual positron emitter nuclei with long half-lives, and the contributions to activity distributions of $^{16}O_{virtual}$ nuclei and activity distributions of $^{40}Ca_{virtual}$ nuclei were only a few percent.

The kinds of nuclei that contributed to measured activity data could be inferred from the approximated half-lives shown in Table I. T_{long} and T_{short} were about 20 min and 20 s for the approximate results of measured activity data of $^{12}C_{virtual}$ nuclei, respectively, which suggested the existence of ^{11}C nuclei and ^{10}C nuclei. From T_{long} being around 20 min, the measured activity data of $^{16}O_{virtual}$ nuclei might have mainly been contributed to by ^{11}C nuclei and various generated positron emitter nuclei such as ^{13}N nuclei (half-life: about 10 min). In addition, from T_{short} being around 130 s, it was estimated that many ^{15}O nuclei and a few other nuclei contributed to the measured activity data of $^{16}O_{virtual}$ nuclei. As for the results of $^{40}Ca_{virtual}$ nuclei, the existence of ^{38}K nuclei (half-life: about 8 min) was suggested from T_{long} being about 10 min and that of ^{38}Ca nuclei (half-life: 0.45 s) and ^{39}Ca nuclei (half-life: 0.86 s) from T_{short} being 1 s. The nuclei whose half-lives were under 1 s, such as ^{38}Ca nuclei and ^{39}Ca nuclei, were both approximated as one nuclei whose half-life was 1 s because the output of the measurement using BOLPs-RGp was every 1 s. In these circumstances, it is easy to distinguish the nuclei with short half-lives from the virtual positron emitter nuclei because half-lives of the generated positron emitter nuclei, which were classified as the virtual positron emitter nuclei with short half-lives, were especially short. It could be considered that the approximate accuracy of the elements with short half-lives was high for the reasons stated above.

Figure 6 shows plots of parameter, $A_{T_{long}}, A_{T_{short}}$, T_{long}, T_{short}, calculated using Eq. (3) for each target nucleus at 179 MeV proton beam. The activity ratios of $^{12}C_{virtual}$, $^{16}O_{virtual}$, and $^{40}Ca_{virtual}$ nuclei were calculated using Eq. (4)

$$R_{T_{long},T_{short}}(\mathrm{X_{virtual}}; z) \equiv \frac{A_{T_{long},T_{short}}(\mathrm{X_{virtual}})}{N_{act.}(z, t = 0)} = \begin{cases} a(\mathrm{X_{virtual}}) + \dfrac{b(\mathrm{X_{virtual}})}{1 + \left(\dfrac{c(\mathrm{X_{virtual}})}{z}\right)^{k(\mathrm{X_{virtual}})}}, & (\mathrm{X_{virtual}}={}^{12}\mathrm{C_{virtual}}) \\ a(\mathrm{X_{virtual}}) + b(\mathrm{X_{virtual}}) \cdot z^{k(\mathrm{X_{virtual}})}, & (\mathrm{X_{virtual}}={}^{16}\mathrm{O_{virtual}}) \\ a(\mathrm{X_{virtual}}). & (\mathrm{X_{virtual}}={}^{40}\mathrm{Ca_{virtual}}) \end{cases} \quad (4)$$

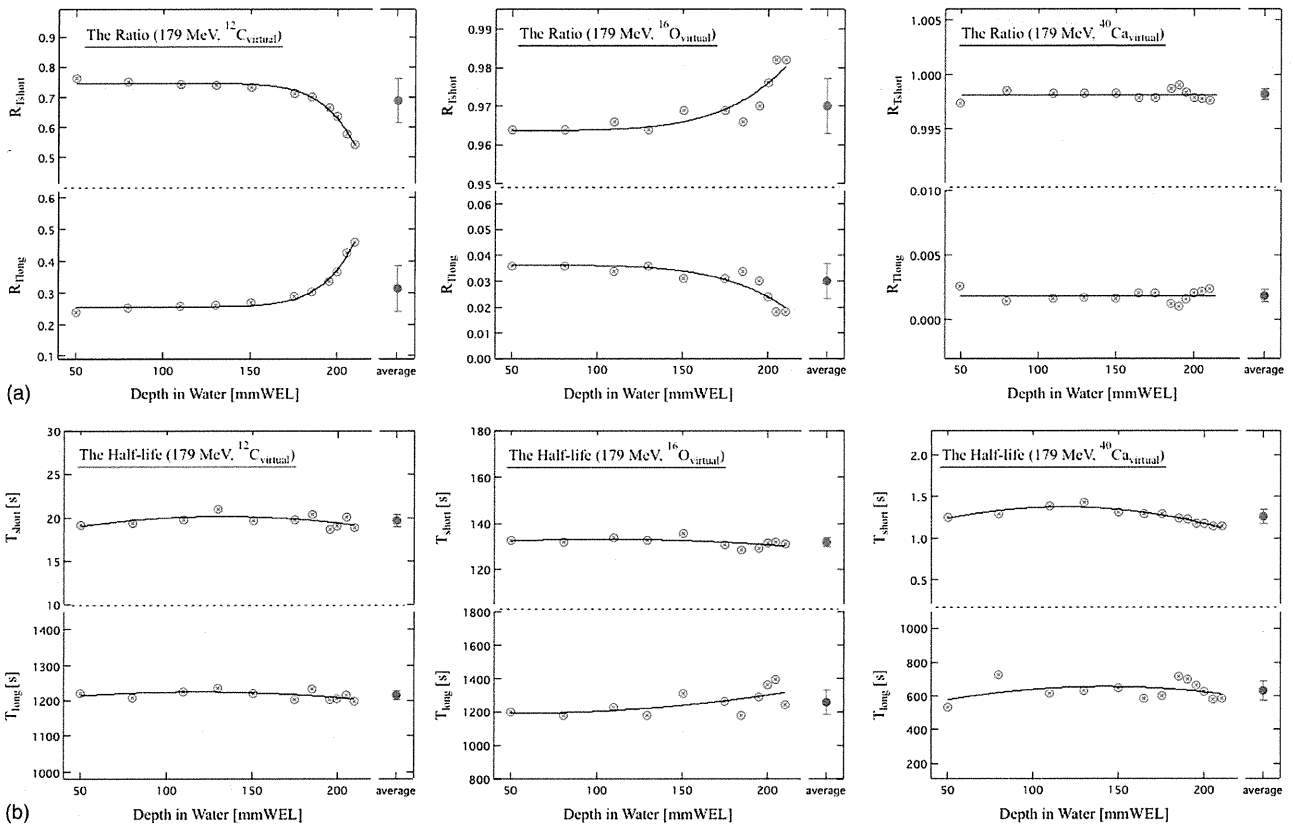

FIG. 6. The plotted points were the results that were the ratio of each half-life group of elements (a) and the hail-lives (b) approximated using Eq. (3) for each virtual positron emitter nuclei at 179 MeV. The curves approximated the results of approximation using Eqs. (4) and (5).

Here, $R_{T_{long},T_{short}}$ is the ratio of $X_{virtual}$ nucleus with each half-life element, and a, b, c, k are free parameters for fitting of data in each equation. The measured activity distributions of $^{40}Ca_{virtual}$ nuclei were mainly formed by the elements of short half-lives according to the result of ratio of ^{40}Ca nuclei half-life elements (see Table I). The half-lives both long and short were calculated using Eq. (5) for each virtual positron emitter nuclei.

$$T_{long,short}(X_{virtual}; z) = a(X_{virtual}) + b(X_{virtual}) \cdot z + c(X_{virtual}) \cdot z^2. \quad (5)$$

Here, $T_{long,short}$ is each half-life of $X_{virtual}$ nucleus. Table II shows the fitting results for each target and energy. The values that were obtained from measured activity data were widely distributed because the analysis volume was set up as small as possible to verify the depth dependence. This could explain why the points that were the results of that analysis are diffusely spread in Fig. 6. Therefore, the change of the form of depth activity distributions with the depth dependence was considered by using of the Eqs. (4) and (5) decided by the results of each target nucleus in this study.

Three nuclei, ^{12}C, ^{16}O, and ^{40}Ca, were proposed to be the main components related to the imaging of proton-irradiated volume in a patient body in this study. It was found that the elements with a short half-life for each target nucleus mainly affected the activity distributions of virtual positron emitter nuclei obtained by proton irradiation to all target nuclei. In other words, it was suggested that the activity distributions obtained by proton irradiation of human body tissues, which were regarded as being mainly composed of ^{12}C nuclei, ^{16}O nuclei, and ^{40}Ca nuclei, were approximated by three half-life elements. It was reported that the activity distributions obtained by proton irradiation of human body tissues in clinical therapy could be approximated by three half-life elements, as found in our previous study.[2] It could be said that the results of this study to analyze three target nuclei (^{12}C, ^{16}O, and ^{40}Ca) have a strong relationship to the results of the previous study on clinical data.

III.C. Activity pencil beam kernel using measured depth activity distributions

Activity pencil beam kernel was constructed by the measured depth activity distribution data of virtual positron emitter nuclei and calculated lateral distributions of Gauss form considering the effect of multiple Coulomb scattering. The measured depth activity distribution data included the influence of time and depth dependence. Form of activity pencil beam kernel was decided by each energy of incident proton beam and each nucleus of ^{12}C, ^{16}O, and ^{40}Ca. And, the data were prepared for installing the simulation system of activity distributions. Figure 7 shows calculation results of the activity pencil beam kernel of $^{12}C_{virtual}$, $^{16}O_{virtual}$, and $^{40}Ca_{virtual}$ nuclei with mono-energetic proton beam of 179 MeV. There

TABLE II. The results of approximation using Eqs. (4) and (5) for each target and energy.

		$R_{T_{long}}$			
Target	Energy [MeV]	a	b	c	k
^{12}C	223	0.262	0.124	301.3	33.9
	179	0.255	2.757	258.0	12.2
	138	0.274	3.471	185.1	8.3
		a	b	k	
^{16}O	223	0.040	0.000	5.1	
	179	0.036	0.000	5.8	
	138	0.044	0.000	5.9	
		Constant Value			
^{40}Ca	223	0.003			
	179	0.002			
	138	0.002			

		$R_{T_{short}}$			
Target	Energy [MeV]	a	b	c	k
^{12}C	223	0.604	0.134	303.4	−31.3
	179	−0.888	1.633	244.8	−12.6
	138	−1.811	2.537	177.0	−8.4
		a	b	k	
^{16}O	223	0.960	0.000	5.1	
	179	0.964	0.000	5.8	
	138	0.956	0.000	5.9	
		Constant Value			
^{40}Ca	223	0.997			
	179	0.998			
	138	0.998			

		T_{long}		
Target	Energy [MeV]	a	b	c
^{12}C	223	1194.5	0.448	−0.002
	179	1192.7	0.531	−0.002
	138	1216.8	−0.308	0.002
^{16}O	223	1085.6	4.778	−0.014
	179	1210.5	−0.588	0.005
	138	1113.1	−2.343	0.019
^{40}Ca	223	813.3	−2.870	0.007
	179	471.1	2.593	−0.009
	138	578.5	0.402	−0.004

		T_{short}		
Target	Energy [MeV]	a	b	c
^{12}C	223	16.4	0.081	0.000
	179	17.2	0.045	0.000
	138	17.7	0.031	0.000
^{16}O	223	139.6	0.078	0.000
	179	130.5	0.052	0.000
	138	129.1	−0.114	0.001
^{40}Ca	223	1.4	0.001	0.000
	179	1.0	0.007	0.000
	138	1.1	0.000	0.000

are four graphs of depth activity distributions, coefficient of multiple Coulomb scattering to depth (1σ), two-dimensional activity pencil beam kernel, and depth activity distributions toward the distance from the central proton beam axis shown in Fig. 7.

The pencil beam algorithm takes into consideration the way in which the center of the proton beam passes through inhomogeneous material in calculation of proton dose distribution. However, lateral Gaussian distribution only represents the scatter in water with no density gap. The accuracy of calculation deteriorates at the point with a large density gap in the inhomogeneous area composed of matter with various densities, such as bone and air. The same phenomenon occurs in the APB algorithm. On the other hand, research to improve the accuracy of the pencil beam algorithm has been carried out worldwide. Calculation using the pencil beam algorithm is being developed to a higher level of accuracy. For instance, research is being carried out on the development of the calculation algorithm with high accuracy on the border of inhomogeneous matter by regarding a scattered beam after passing fine degrader and bolus as a thin beam.[27] The calculation accuracy of activity distributions using the APB algorithm is the same as the calculation accuracy of dose distributions in clinical proton therapy. Therefore, it is evaluated that the calculation accuracy using the APB algorithm satisfies the accuracy required in clinical use. With progress in the research and development on improving the accuracy of dose calculation, mainly using the pencil beam algorithm, it is certain that the accuracy of activity distribution calculation using the APB algorithm will also be improved. In these circumstances and given these future possibilities, it will be very valuable for calculation of activity distributions to utilize the pencil beam algorithm.

III.D. Sorting CT image of patients into composite nuclear image in a human body for simulation of activity distributions

In proton dose calculation, the physical process of a proton beam passing into a human body is based on electromagnetic interaction, which is mainly proportional to the ionization potential of matter depended on the atomic number Z. In addition, the CT value of a CT image taken for the physical reactions of Photoelectric effect and Compton scattering between a human body and x-ray of about 100 kV depends on the electron density of matter depended on Z. Using these relationships with Z, proton dose distributions are calculated using CT image of patient for treatment planning in clinical proton therapy. On the other hand, target nuclear fragment reactions, which are nuclear reactions between atomic nuclei that constitute a human body and proton in proton therapy, are related to the atomic number Z and the mass number A, as an nucleus is identified by these factors of Z and A. Therefore, sorting the CT image of patients into nuclei is essential to simulate imaging of the planned irradiation volume, although it is suggested that calculation with high speed and high accuracy using APB algorithm can be used in a clinical routine. The best approach is

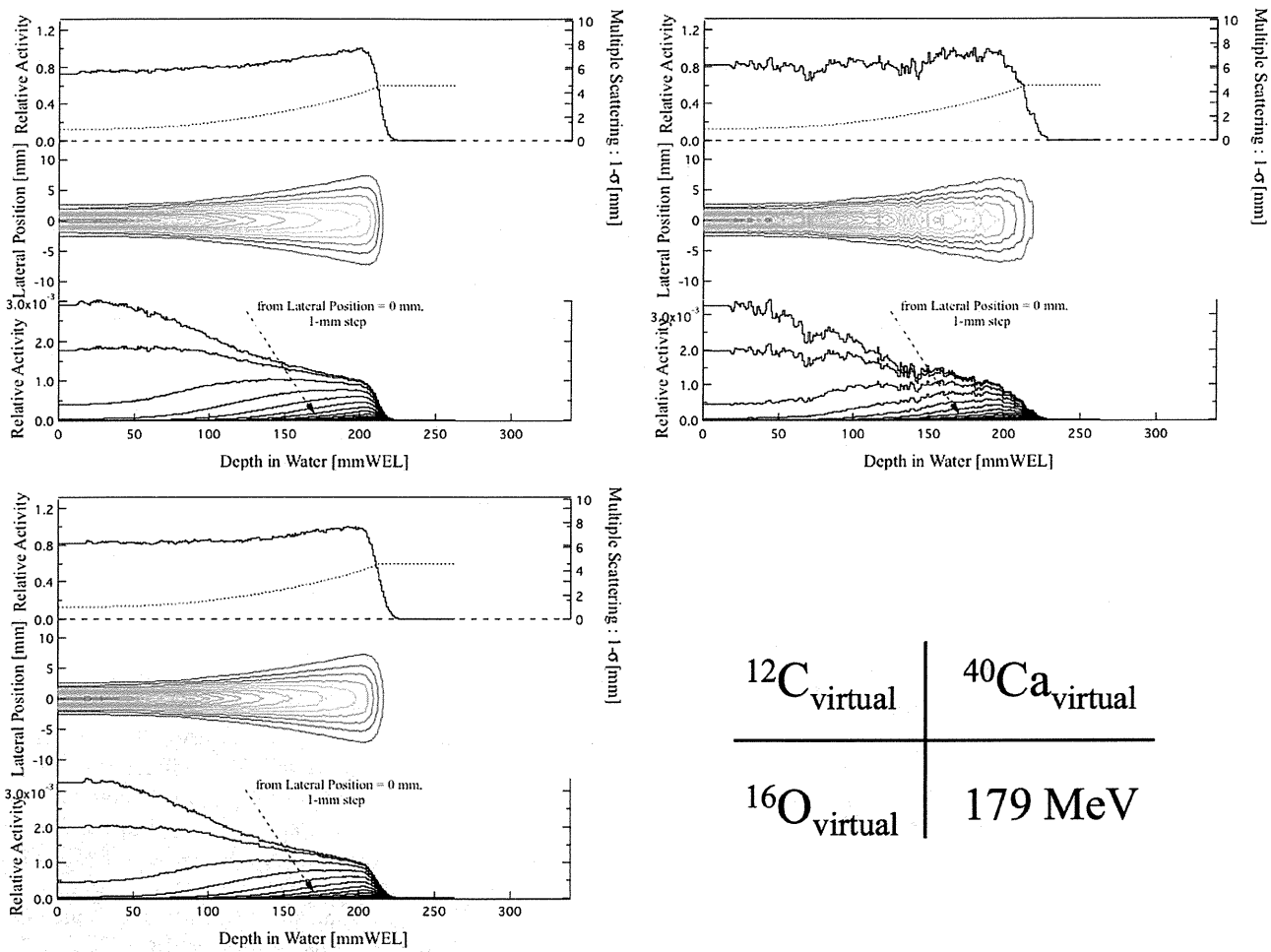

FIG. 7. The results of calculated activity pencil beam kernel of $^{12}C_{virtual}$, $^{16}O_{virtual}$, and $^{40}Ca_{virtual}$ nuclei with mono-energetic proton beam of 179 MeV. There are four graphs, the upper: depth activity distributions and coefficient of multiple Coulomb scattering to depth (1σ), the middle: two-dimensional activity pencil beam kernel, the lower: depth activity distributions toward the distance from the central proton beam axis.

that sorting of CT images into nuclei is done on an individual patient because the composition of human body tissue differs among individuals. However, such a technique has not been established yet. The accuracy of identifying human body tissue from CT values affects the accuracy of dose calculation in proton therapy.[28,29] Research on the relationship between CT value and human body tissue to improve the accuracy of dose and activity calculations in proton therapy has been continuously done.[15,16,29–33] The accuracy of identifying nuclei in the human body from CT images has a strong relationship to the accuracy of the whole simulation of imaging of the planned irradiation volume. Therefore, which technique of identification is to be chosen is an issue to be resolved.

IV. CONCLUSIONS

The APB algorithm that has both the accuracy and the calculation time required for clinical use was developed as a new calculation algorithm for the simulation of activity distributions. It was expected that a simulation system with the APB algorithm for making activity distributions of irradiated volume in patient body using activity pencil beam kernel could be put into clinical use.

It was found that three target nuclei, ^{12}C, ^{16}O, and ^{40}Ca, were important and appropriate for calculation of activity distributions by verification and analysis of clinical data in this study. In terms of the information of target nuclear fragment reactions between proton and nuclei in a human body required for calculation of activity distributions, the information of reactions was enriched with the measured data of the generated virtual positron emitter nuclei to improve the accuracy of simulation of activity distributions. Acquisition of the data of target nuclear fragment reactions between ^{40}Ca nuclei and proton within the range of energy used for proton therapy in this study was very useful because such data are limited at present. Moreover, high accurate proton therapy can be provided by the development of a new calculation algorithm considering the time and depth dependence of the forms of activity distributions.

We have been constructed a simulation system of imaging of proton-irradiated volume equipped the APB algorithm now. Then, it will be possible to verify the changes of the irradiated volume and the influence of washout effect on

images of activity distributions by comparing the results of calculation with measurement using BOLPs-RGp. It is thought that there are many seeds (e.g., *in vivo* dosimetry) of research based on measurement and calculation of activity in irradiated volume. The accuracy of activity distribution calculation using APB algorithm is future problem. Therefore, it will be important for verification of measured activity distribution using BOLPs-RGp and calculated activity distribution using APB algorithm in clinical cases. It is expected that the APB algorithm can be utilized for proton therapy with imaging of irradiated volume. We will be able to provide high quality proton therapy for patients.

ACKNOWLEDGMENTS

The authors would like to thank T. Okamoto of Hamamatsu Photonics K. K., H. Oka and K. Tojima of MED-1 Asia Japan, Ltd., for technical support. They also thank the staff members of the Proton Radiotherapy Department of National Cancer Center, Kashiwa, for their help, the members of SHI Accelerator Service, Ltd., and Accelerator Engineering, Inc., for the operation of the proton apparatus. This work was supported by Health and Labour Science Research Grants from the Japanese Government.

[a]Electronic mail: miyatake.keenmps@gmail.com

[1]T. Nishio, A. Miyatake, T. Ogino, K. Nakagawa, N. Saijo, and H. Esumi, "The development and clinical use of a beam ON-LINE PET system mounted on a rotating gantry port in proton therapy," Int. J. Radiat. Oncol., Biol., Phys. **76**, 277–286 (2010).

[2]A. Miyatake, T. Nishio, T. Ogino, N. Saijo, H. Esumi, and M. Uesaka, "Measurement and verification of positron emitter nuclei generated at each treatment site by target nuclear fragment reactions in proton therapy," Med. Phys. **37**, 4445–4455 (2010).

[3]G. W. Bennett, A. C. Goldberg, G. S. Levine, J. Guthy, and J. Balsamo, "Beam localization via 15O activation in proton-radiation therapy," Nucl. Instrum. Methods **125**, 333–338 (1975).

[4]U. Oelfke, G. Lam, and M. Atkins, "Proton dose monitoring with PET: Quantitative studies in Lucite," Phys. Med. Biol. **41**, 177–196 (1996).

[5]D. W. Litzenberg, D. A. Roberts, M. Y. Lee, K. Pham, A. M. Vander Molen, R. Ronningen, and F. D. Becchetti, "On-line monitoring of radiotherapy beams: Experimental results with proton beams," Med. Phys. **26**(6), 992–1006 (1999).

[6]T. Nishio, T. Ogino, M. Shimbo, S. Katsuta, S. Kawasaki, T. Murakami, T. Sato, Y. Kojima, K. Murakami, and H. Ikeda, "Distributions of β^+ decayed nucleus produced from the target fragment reaction in $(CH_2)n$ and patient liver targets by using a proton beam for therapy," *Abstracts of the XXXIV PTCOG MEETING in Boston*, p. 15–16 (2001).

[7]Y. Hishikawa, K. Kagawa, M. Murakami, H. Sasaki, T. Akagi, and M. Abe, "Usefulness of positron-emission tomographic images after proton therapy," Int. J. Radiat. Oncol., Biol., Phys. **53**, 1388–1391 (2002).

[8]W. Enghardt, P. Crespo, F. Fiedler, R. Hinz, K. Parodi, J. Pawelke, and F. Ponisch, "Dose quantification from in-beam positron emission tomography," Radiother. Oncol. **73**, Suppl. 2. S96–98 (2004).

[9]T. Nishio, T. Sato, H. Kitamura, K. Murakami, and T. Ogino, "Distributions of β^+ decayed nuclei generated in the CH_2 and H_2O targets by the target nuclear fragment reaction using therapeutic MONO and SOBP proton beam," Med. Phys. **32**(4), 1070–1082 (2005).

[10]T. Nishio, T. Ogino, K. Nomura, and H. Uchida, "Dose-volume delivery guided proton therapy using beam ON-LINE PET system," Med. Phys. **33**(11), 4190–4197 (2006).

[11]T. Nishio, A. Miyatake, K. Inoue, S. Katsuta, T. Gomi-Miyagishi, R. Kohno, S. Kameoka, K. Nakagawa, and T. Ogino, "Experimental verification of proton beam monitoring in a human body by use of activity image of positron-emitting nuclei generated by nuclear fragmentation reaction," Radiol. Phys. Technol. **1**(1), 44–54 (2008).

[12]K. Parodi and W. Enghardt, "Potential application of PET in quality assurance of proton therapy," Phys. Med. Biol. **45**, N151–N156 (2000).

[13]K. Parodi, W. Enghardt, and T. Haberer, "In-beam PET measurements of β^+ radioactivity induced by proton beams," Phys. Med. Biol. **47**, 21–36 (2002).

[14]K. Parodi, F. Ponisch, and W. Enghardt, "Experimental study on the feasibility of in-beam PET for accurate monitoring of proton therapy," IEEE Trans. Nucl. Sci. **52**, 778–786 (2005).

[15]K. Parodi, H. Paganetti, H. A. Shih, S. Michaud, J. S. Loeffler, T. F. Delaney, N. J. Liebsch, J. E. Munzenrider, A. J. Fischman, A. Knopf, and T. Bortfeld, "Patient study of in vivo verification of beam delivery and range, using positron emission tomography and computed tomography imaging after proton therapy," Int. J. Radiat. Oncol., Biol., Phys. **68**(3), 920–934 (2007).

[16]K. Parodi, H. Paganetti, E. Cascio, J. B. Flanz, A. A. Bonab, N. M. Alpert, K. Lohmann, and T. Bortfeld, "PET/CT imaging for treatment verification after proton therapy: A study with plastic phantoms and metallic implants," Med. Phys. **34**(2), 419–435 (2007).

[17]K. Parodi, A. Ferrari, F. Sommerer, and H. Paganetti, "Clinical CT-based calculations of dose and positron emitter distributions in proton therapy using the FLUKA Monte Carlo code," Phys. Med. Biol. **52**, 3369–3387 (2007).

[18]S. Agostinelli *et al.*, "(GEANT4 Collaboration) 2003 GEANT4: a simulation toolkit," Nucl. Instrum. Methods Phys. Res. A **506**, 250–303 (2003).

[19]J. Allison *et al.*, "(GEANT4 Collaboration) 2006 GEANT4 developments and applications," IEEE Trans. Nucl. Sci. **53**, 270–278 (2006).

[20]A. Fassò, A. Ferrari, J. Ranft, and P. Sala, FLUKA-98 (http://www.oecd-nea.org/science/iend.hide/iend_20.pdf) (1998).

[21]F. Ponisch, K. Parodi, B. G. Hasch, and W. Enghardt, "The modelling of positron emitter production and PET imaging during carbon ion therapy," Phys. Med. Biol. **49**, 5217–5232 (2004).

[22]NNDC : http://www.nndc.bnl.gov./

[23]G. Moliere, "Theorie der Streuung schneller geladener Teilchen II," Nucl. Instrum. Methods Phys. Res. B **74**, 467–490 (1948).

[24]L. V. Highland, "Some practical remarks on multiple scattering," Nucl. Instr. Methods **129**, 467–499 (1975).

[25]R. G. Lynch and I. O. Dahl, "Approximations to multiple Coulomb scattering," Nucl. Instrum. Methods Phys. Res. B **58**, 6–10 (1991).

[26]M. Hollmark *et al.*, "Influence of multiple scattering and energy loss straggling on the absorbed dose distributions of therapeutic light ion beams: I. Analytical pencil beam model," Phys. Med. Biol. **49**, 3247–3265 (2004).

[27]N. Kanematsu, "Semi-empirical formulation of multiple scattering for the Gaussian beam model of heavy charged particles stopping in tissue-like matter," Phys. Med. Biol. **54**, N67–N73 (2009).

[28]B. Schaffner and E. Pedroni, "The precision of proton range calculations in proton radiotherapy treatment planning: experimental verification of the relation between CT-HU and proton stopping power," Phys. Med. Biol. **43**, 1579–1592 (1998).

[29]H. Jiang, J. Seco, and H. Paganetti, "Effects of Hounsfield number conversions on patient CT based Monte Carlo proton dose calculation," Med. Phys. **34**, 1439–1449 (2007).

[30]H. Jiang and H. Paganetti, "Adaptation of GEANT4 to Monte Carlo dose calculations based on CT data," Med. Phys. **31**, 2811–2818 (2004).

[31]H. Paganetti, H. Jiang, K. Parodi, R. Slopsema, and M Engelsman, "Clinical implementation of full Monte Carlo dose calculation in proton beam therapy," Phys. Med. Biol. **53**, 4825–4853 (2008).

[32]H. Paganetti, "Dose to water versus dose to medium in proton beam therapy," Phys. Med. Biol. **54**, 4399–4421 (2009).

[33]S. Espana and H. Paganetti, "The impact of uncertainties in the CT conversion algorithm when predicting proton beam ranges in patients from dose and PET-activity distributions," Phys. Med. Biol. **55**, 7557–7571 (2010).

Int. J. Radiation Oncology Biol. Phys., Vol. 81, No. 1, pp. 135–139, 2011

0360-3016/$–see front matter

ELSEVIER

doi:10.1016/j.ijrobp.2010.04.071

CLINICAL INVESTIGATION **Head and Neck**

PROTON BEAM THERAPY AS A NONSURGICAL APPROACH TO MUCOSAL MELANOMA OF THE HEAD AND NECK: A PILOT STUDY

SADAMOTO ZENDA, M.D., MITSUHIKO KAWASHIMA, M.D., TEIJI NISHIO, PH.D., RYOSUKE KOHNO, PH.D., KEIJI NIHEI, M.D., PH.D, MASAKATSU ONOZAWA, M.D, SATOKO ARAHIRA, M.D, AND TAKASHI OGINO, M.D.

Division of Radiation Oncology, National Cancer Center Hospital East, Kashiwa, Chiba, Japan

Purpose: The aim of this pilot study was to assess the clinical benefit of proton beam therapy for mucosal melanoma of the head and neck.
Methods and Materials: Patients with mucosal melanoma of the head and neck with histologically confirmed malignant melanoma and N0 and M0 disease were enrolled. Proton therapy was delivered three times per week with a planned total dose of 60 Gy equivalents (GyE) in 15 fractions.
Results: Fourteen consecutive patients were enrolled from January 2004 through February 2008. Patient characteristics were as follows: median age 73 years old (range, 56 to 79 years); male/female ratio, 7/7; and T stage 1/2/3/4, 3/2/0/9. All patients were able to receive the full dose of proton therapy. The most common acute toxicities were mucositis (grade 3, 21%) and mild dermatitis (grade 3, 0%). As for late toxicity, 2 patients had a unilateral decrease in visual acuity, although blindness did not occur. No treatment-related deaths occurred throughout the study. Initial local control rate was 85.7%, and, with a median follow-up period of 36.7 months, median progression-free survival was 25.1 months, and 3-year overall survival rates were 58.0%. The most frequent site of first failure was cervical lymph nodes (6 patients), followed by local failure in 1 patient and lung metastases in 1 patient. On follow-up, 5 patients died of disease, 4 died due to cachexia caused by distant metastases, and 1 patient by carotid artery perforation cause by lymph nodes metastases.
Conclusions: Proton beam radiotherapy showed promising local control benefits and would benefit from ongoing clinical study. © **2011 Elsevier Inc.**

Proton beam therapy, Mucosal melanoma, Head and neck.

INTRODUCTION

Although rare worldwide, mucosal melanoma of the head and neck is relatively common in Japan (1). Most reports to date have described small series of patients over long time periods but have not led to any consensus in the approach to treatment. A surgical approach incorporating postoperative radiotherapy has been recognized as a community standard, and the 5-year survival rate of head and neck mucosal melanoma varies from 20% to 45% (2–5). This surgical approach is often complicated by serious cosmetic and functional deformity, and, particularly for nasal and sinonasal mucosal melanoma, satisfactory surgical clearance is often markedly difficult to obtain.

Several reports have described the use of radiotherapy alone for mucosal melanoma of the head and neck, with 5-year survival rates slightly less than those of the surgical approach (6–8). Regarding radiotherapy, The review by Trotti *et al.* (9) of four reports of radiotherapy for mucosal melanoma showed 3-year local control rates of 36% to 61%. In Japan Wada *et al.* (10) recently reported a series of 66 cases of mucosal melanoma of the head and neck, 21 of whom were treated with radiotherapy as the main modality. The rate of complete response in these 21 cases was 29%, and the 3-year disease-specific survival rate was 33%. Since X-ray irradiation has a limitation of dose distribution for tumor areas in proximity to organs at risk, like optic nerve and brain stem, it is often difficult to give enough dosage to planned target volume.

Proton beam therapy (PBT) is characterized by rapid fall-off at the distal end of the Bragg peak and a sharp lateral penumbra, depending on the energy, depth, and delivery (11).

Because of its physical characteristics, PBT provides better dose distribution than X-ray irradiation. PBT is deemed a feasible and effective treatment modality that provides curative high-dose irradiation to the tumor volume without increasing normal tissue toxicity. However, the use of PBT

Reprint requests to: Sadamoto Zenda, M.D., Division of Radiation Oncology, National Cancer Center Hospital East, 6-5-1 Kashiwanoha, Kashiwa, Chiba 277-8577, Japan. Tel: (+81) 4-7133-1111; Fax: (+81) 4-7131-9960; E-mail: szenda@east.ncc.go.jp

Conflict of interest: none.
Received Nov 18, 2009, and in revised form March 3, 2010. Accepted for publication April 29, 2010.

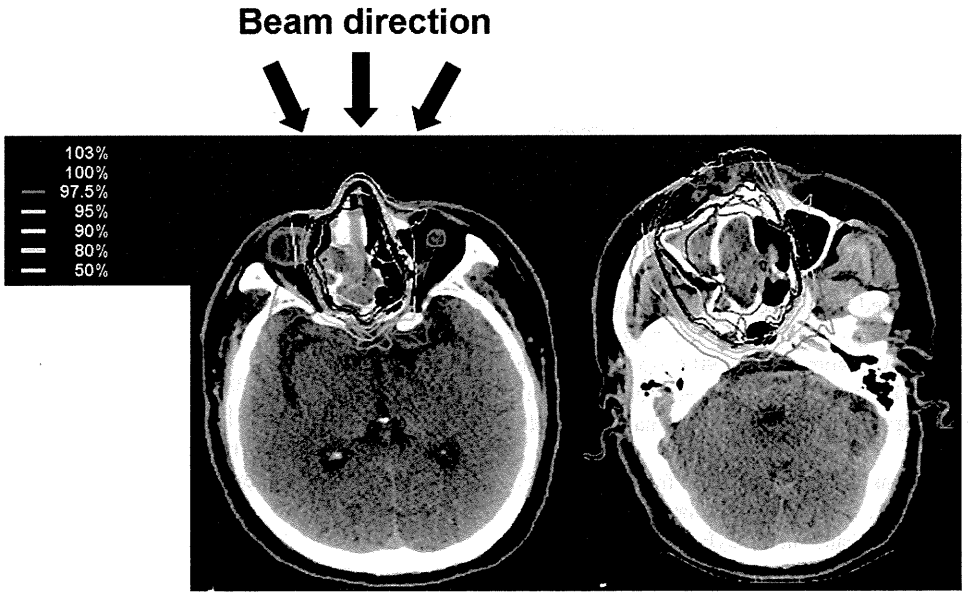

Fig. 1. Target volume and beam arrangement. GTV was defined as the gross tumor lesion determined with pretreatment CT/MRI and PET. CTV was defined as the region of the gross tumor lesion and adjacent sinuses. PTV was basically set as CTV plus 3-mm margin, with acceptance of fine-tuning to the PTV in consideration of organs at risk. Irradiation dose and volume for organs at risk were usually minimized by using a noncoplanar three-field technique.

for mucosal melanoma of the head and neck has not been reported. Here, we conducted a pilot study to examine the utility of hypofractionated PBT as a newly developed treatment modality for mucosal melanoma of the head and neck.

METHODS AND MATERIALS

Patients

Entry criteria for this retrospective study were (*1*) pathologically proven mucosal melanoma of the head and neck; (*2*) clinical TNM status of N0M0; (*3*) Eastern Cooperative Oncology Group (ECOG) performance status of 2 or less; (*4*) adequate organ function; and (*5*) no active concomitant malignancy. This treatment was approved by the institutional review board of the National Cancer Center Hospital, and written informed consent to treatment was obtained from all patients before the initiation of treatment.

Pretreatment clinical evaluation was performed using magnetic resonance imaging (MRI); cervical, chest, and abdominal computed tomography (CT); and/or positron emission tomography-CT (PET-CT). Radiological evaluations for staging were jointly reviewed by radiologists, surgeons, and oncologists at our institution. In the present study, all diseases were staged with the International Union Against Cancer criteria for carcinoma of the nasal cavity or paranasal sinus (12).

Table 1. Patient characteristics

Characteristic	Parameter	No. of patients (n = 14)
Age	Median (range)	73 (56-79)
Gender	Male/female	7/7
Performance Status	0 to 1/2	14/0
Primary site	Nasal cavity	11
	Paranasal sinus	3
TNM stage	T1N0M0	3
	T2N0M0	2
	T3N0M0	0
	T4N0M0	9

Treatment

PBT was delivered three times per week for a planned total dose of 60 Gy equivalents (GyE) in 15 fractions using a 150- to 190-MeV proton beam. The biologically equivalent dose (BED) using a linear-quadratic model is defined as BED = nd [1+ d/1/(α/β)], where n is the fractionation number, d is the daily dose, and the α/β ratio was 2.5 ($Gy_{2.5}$) for malignant melanomas (6). When n = 15 and d = 4 were substituted, BED was 156 $Gy_{2.5}$.

Treatment planning was performed with a three-dimensional CT planning system. In this system, the proton beam was generated with a Cyclotron C235 with an energy of 235 MeV at the exit. Relative biologic effectiveness was defined as 1.1, based on our preclinical

Table 2. Adverse events

	No. of patients with toxicity grade shown*				
Toxicity	1	2	3	4	% 3-4
Dermatitis	7	5	0	0	0
Mucositis	9	2	3	0	21
Infection	0	0	0	0	0
Hearing loss	1	0	0	0	0
Neuropathy					
CN-II	0	0	2	0	12
CN-V	0	0	0	0	0
Keratitis	0	2	0	0	0
Memory impairment	0	0	0	0	0

Treatment-related death: 0%.

* Using Common Terminology Criteria for Adverse Events vesion.3.0.

experiments (13). PBT at our institution is passive irradiation with dual-ring double-scatter methods. Dose distribution was optimized using the spread-out Bragg peak method and obtained using a broad-beam algorithm.

Gross tumor volume (GTV) was determined with pretreatment CT, MRI, and/or PET-CT. The clinical target volume (CTV) was defined as the GTV plus a 5-mm margin and sinuses adjacent to GTV. In cases with brain invasion, the area of T_2-weighted prolongation on MRI was also included in the CTV. The planning target volume (PTV) was basically defined as the CTV plus a 3-mm margin but could be finely adjusted where necessary in consideration of organs at risk. The beam energy and spread-out Bragg peak were fine-tuned such that the PTV encompassed a 90% isodose volume of the prescribed dosage. Irradiation dose and volume for organs at risk was usually minimized using a noncoplanar three-field technique (Fig. 1).

Dose constraints for organs at risk at 4 GyE per fraction were (*1*) surface of brainstem, 45 GyE; (*2*) center of brainstem, 33 GyE; (*3*) optic nerves of the healthy side/chiasm, 42 GyE; and (*4*) optic lens, 13 GyE.

To evaluate the risk of radiation-induced complications in normal tissue, dose–volume histograms were calculated for all patients. Patients were immobilized with custom-made immobilization devices that provided high reproducibility at every treatment fraction. Patient setup was verified before the delivery of each fraction, using a digital radiography subtraction system.

Evaluation of toxicity and efficacy

Toxicities were graded using the Common Terminology Criteria for Adverse Events (CTCAE) version 3.0. Weekly follow-up was continued until acute toxicity was easily manageable, and posttreatment MRI was performed at 6 to 10 weeks after the end of PBT to rule out treatment-induced empyema and brain necrosis. To confirm local control, MRI was performed every 3 to 6 months after the end of treatment, and distant metastases were assessed by CT/PET-CT. The achievement of initial local control was confirmed when all of the following criteria were fulfilled: (*1*) patients were alive at 1 year after the initiation of treatment; (*2*) no progressive disease was detected at the primary site for 1 year; and (*3*) no recurrence was detected at the primary site for 1 year.

Statistical analysis

Overall survival time was calculated from the start of treatment to the date of death or last confirmed date of survival. Survival time was censored at the last confirmed date of survival if the patient was alive. Progression-free survival (PFS) time was defined from the day of initiation of treatment to the first day of confirmation of progressive disease at any site or any cause of death. Overall survival time, PFS time, and local control period were estimated using the Kaplan-Meier product-limits method.

RESULTS

Patient characteristics

Fourteen consecutive patients with mucosal melanoma of the head and neck were treated with PBT at the National Cancer Center East from March 2004 through February 2007. All patients agreed to participate in the present study. Patient characteristics are listed in Table 1. Median age was 72 years (range, 56 to 79 years). Most patients had a good performance status, and over half the patients had T4 disease.

Toxicity

Major adverse reactions to PBT are listed in Table 2. The most common acute toxicities were mucositis (grade 3, 21%) and mild dermatitis (grade 3, 0%). All patients were able to receive the full dose of PBT (60 GyE) given with a median duration of 36 days (range, 33–42 days). Blindness did not occur, although 2 patients had a unilateral decrease in visual acuity. No treatment-related deaths occurred throughout the study.

Efficacy

Initial local control rate was 85.7% (12/14 patients, 95% confidence interval [CI], 57.2%–98.2%). One patient had recurrent disease, and 1 patient died within 1 year after the initiation of treatment.

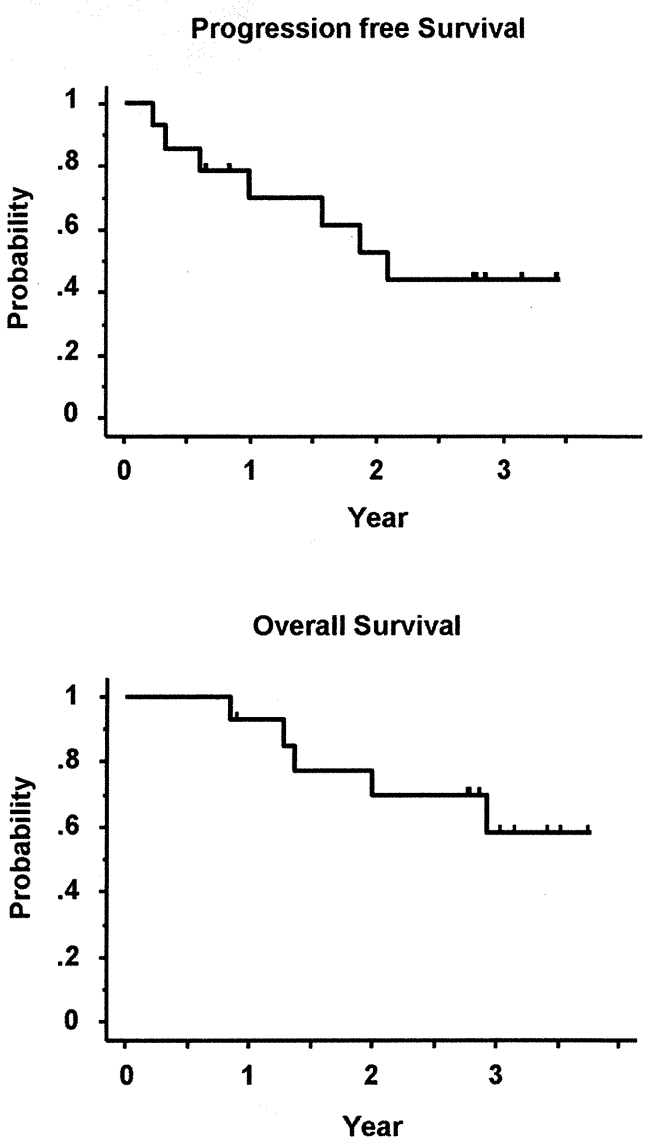

Fig. 2. Progression-free survival (PFS) and overall survival (OS). PFS and OS rates were estimated using the Kaplan-Meier product-limits method. Median PFS was 25.1 months, and 2-year PFS rates were 43.7%. Median survival time was not reached, and 3-year overall survival rate was 58.0% with a follow-up period of 36.7 months.

Table 3. Failure pattern in detail

Case	Time to failure	Failure site	Second-line treatment	Status (time)	Cause of death
1	2.7 M	LN II	Observation	Alive (35.2 M)	
2	22.5 M	LN Ib	Salvage Surgery	Death (35.1 M)	DOD/LM
3	3.8 M	LN Ib, II	Observation	Death (15.4 M)	DOD/DM
6	30.1 M	LN Ib, II	Salvage Surgery	Alive (37.0 M)	
8	11.9M	LN II	Radiation	Death (18.6 M)	DOD/DM
9	7.1 M	LN Ib, II	Salvage Surgery	Death (23.9 M)	DOD/DM
10	8.1 M	Lung	Observation	Death (10.1 M)	DOD/DM
11	18.6 M	Primary site	Observation	Alive (42.7 M)	

Abbreviations: M = months; LN = lymph node; DOD = died of disease; LM = lymph node metastases; DM = distant metastases.

Median PFS was 25.1 months, and 2-year PFS rate was 43.7%. Median survival time with a follow-up period of 36.7 months was not reached, and 3-year overall survival rate was 58.0% (Fig. 2).

Failure pattern and second-line treatment

Six of 14 patients were alive at the end of follow-up with no evidence of disease, while the remaining 8 patients had evidence of disease progression. The most frequent site of first failure was a cervical lymph node outside of the PTV (6/8 patients), followed by local failure in 1 patient (1/8), and lung metastases in one patient (1/8). Failure pattern details are shown in Table 3. With regard to lymph node metastases, 4 patients (4/6) experienced progress within 1 year, and all failure sites were lymph node level Ib or II.

Cause of death

On follow-up, 5 patients died of disease, 4 patients due to cachexia caused by distant metastases and 1 patient by carotid artery perforation cause by lymph nodes metastases.

DISCUSSION

In this study, hypofractionated PBT showed good local control for mucosal melanoma of the head and neck and acceptable toxicity. Prognosis of mucosal melanoma of the head and neck remains poor. In their review of more than 1,000 patients, Mandolis *et al.* (14) reported 5- and 10-year survival rates of 17% and 5%, respectively. Overgaard *et al.* (6) reported a significant relationship between dose per fraction and response, with complete response rates of 59% when fractions of more than 4 Gy were used, compared to 24% with fractions lower than or equal to 4 Gy, while a univariate analysis by Wada *et al.* (9) revealed that a high dose per fraction (3Gy) and high biologically equivalent total dose were associated with better local control and survival.

From these findings, our treatment schedule was planned with consideration for two premises: hypofractionation and high BED. Carbon ion radiotherapy is a promising nonsurgical modality for mucosal melanoma of the head and neck. Yanagi *et al.* (15) reported that with a median follow-up period of 49.2 months, 3-year survival rates were 46.1% in mucosal melanoma patients treated with carbon ion radiotherapy.

The 3-year overall survival rate was 58.0% in the present study. In comparison with the surgical approach or carbon ion therapy, the efficacy of PBT seemed not to be inferior, although recruiting number of patients was small. With regard to late toxicity, decreased visual acuity occurred in 2 patients. Generally, it is often inevitable that the PTV in stage T4 disease with paranasal and/or intracranial invasion includes the unilateral or bilateral optic nerves. In these patients, the better

Table 4. Published cases of late toxicity

Author (study)	Year	Location	Modality	No.of patients	% Treatment outcome	Late toxicity (severe morbidity)
Owens *et al.* (3)	2003	Sinonasal	S	20	5YSR 45%	Not mentioned
			S + RT	24	5YSR 29%	
Temam *et al.* (4)	2005	Sinonasal +α	S/S + RT	30/39	5YSR 20%	Not mentioned
Krengli Owens *et al.* (5)	2006	Head and neck	S/S + RT/others	17/42/15	3YSR 31%	>Grade 3 11% Stenosis of the nasocrimal duct Dry-eye syndrome Optic nerve toxicity Bone necrosis
Wada Owens *et al.* (10)	2004	Sinonasal +α	RT/S+RT	21/10	3YSR 33%	Grade 4 6% soft tissue necrosis; fatal bleeding
Gilligan and Slevin (7)	1991	(Para)-nasal	RT	28	5YSR 17.9%	None
Yanagi *et al.* (15)	2009	Head and neck	Carbon	72	3YSR 46.1%	Grade 2 skin, mucosa*
Present study	2010	Paranasal	Proton	14	3YSR 58.0%	Gade 3 12% unilateral visual acuity

Abbreviations: 5YSR = 5 year survival rate; S = surgery.
* Visual loss after carbon ion radiotheraphy was not mentioned.

dose distribution characteristics of PBT over X-ray should minimize the risk of treatment-related bilateral visual impairment or treatment-related blindness.

Hasegawa *et al.* (16) showed that a certain degree of visual impairment had occurred in 28% of patients whose optic nerves were included in the irradiated volume in carbon ion radiotherapy. There is no report about a direct comparison between PBT and carbon ion radiotherapy.

Previous reports about various approaches to mucosal melanoma are summarized in Table 4.

Cervical lymph nodes were the most frequent site of first failure, and most patients who died finally had distant metastases. Several authors have suggested that aggressive local treatment should be initiated at the presentation of localized melanomas, on the basis that the achievement of local tumor control may increase in survival rate (6, 17). However, it remains controversial whether cervical lymph nodes should be included in the treatment field. We think that what we can do at present is to institute close follow-up after PBT and to detect signs of recurrence or regrowth as early as possible.

CONCLUSIONS

In conclusion, PBT for mucosal melanoma showed promising local control benefit and enough feasibility. To confirm the efficacy and safety, a phase II study of hypofractionated PBT for mucosal melanoma of the head and neck (UMIN-000001505) using the same treatment schedule as the present study is now ongoing in Japan.

REFERENCES

1. Umeda M, Mishima Y, Teranobu O, *et al.* Heterogeneity of primary malignant melanomas in oral mucosa: an analysis of 43 cases in Japan. *Pathology* 1988;20:234–241.
2. Patel SG, Prasad ML, Escrig M, *et al.* Primary mucosal malignant melanoma of the head and neck. *Head Neck* 2002;24: 247–257.
3. Owens JM, Roberts DB, Myers JN. The role of postoperative adjuvant radiation therapy in the treatment of mucosal melanomas of the head and neck region. *Arch Otolaryngol Head Neck Surg* 2003;129:864–868.
4. Temam S, Mamelle G, Marandas P, *et al.* Postoperative radiotherapy for primary mucosal melanoma of the head and neck. *Cancer* 2005;103:313–319.
5. Krengli M, Masini L, Kaanders JH, *et al.* Radiotherapy in the treatment of mucosal melanoma of the upper aerodigestive tract: Analysis of 74 cases. A Rare Cancer Network study. *Int J Radiat Oncol Biol Phys* 2006;65:751–759.
6. Overgaard J, Overgaard M, Hansen PV, *et al.* Some factors of importance in the radiation treatment of malignant melanoma. *Radiother Oncol* 1986;5:183–192.
7. Gilligan D, Slevin NJ. Radical radiotherapy for 28 cases of mucosal melanoma in the nasal cavity and sinuses. *Br J Radiol* 1991;64:1147–1150.
8. Sause WT, Cooper JS, Rush S, *et al.* Fraction size in external beam radiation therapy in the treatment of melanoma. *Int J Radiat Oncol Biol Phys* 1991;20:429–432.
9. Trotti A, Peters LJ. Role of radiotherapy in the primary management of mucosal melanoma of the head and neck. *Semin Surg Oncol* 1993;9:246–250.
10. Wada H, Nemoto K, Ogawa Y, *et al.* A multi-institutional retrospective analysis of external radiotherapy for mucosal melanoma of the head and neck in Northern Japan. *Int J Radiat Oncol Biol Phys* 2004;59:495–500.
11. Urie MM, Sisterson JM, Koehler AM, Goitein M, Zoesman J. Proton beam penumbra: Effects of separation between patient and beam modifying devices. *Med Phys* 1986;13:734–741.
12. . Sobin LH, Gospodarowicz MK, Wittekind CH, editors. International Union Against Cancer (UICC): TNM classification of malignant tumors. 7th ed. West Sussex (UK): Wiley-Blackwell; 2010.
13. Ando K, Furusawa Y, Suzuki M, *et al.* Relative biological effectiveness of the 235 MeV proton beams at the National Cancer Center Hospital East. *J Radiat Res (Tokyo)* 2001;42:79–89.
14. Manolidis S, Donald PJ. Malignant mucosal melanoma of the head and neck: Review of the literature and report of 14 patients. *Cancer* 1997;80:1373–1386.
15. Yanagi T, Mizoe JE, Hasegawa A, Takagi R, Bessho H, Onda T, Kamada T, Okamoto Y, Tsujii H. Mucosal malignant melanoma of the head and neck treated by carbon ion radiotherapy. *Int J Radiat Oncol Biol Phys* 2009;1:15–20.
16. Hasegawa A, Mizoe JE, Mizota A, Tsujii H. Outcomes of visual acuity in carbon ion radiotherapy: Analysis of dose-volume histograms and prognostic factors. *Int J Radiat Oncol Biol Phys* 2006;64(2):396–401.
17. Lee SP, Shimizu KT, Tran LM, *et al.* Mucosal melanoma of the head and neck: The impact of local control on survival. *Laryngoscope* 1994;104:121–126.

J. Radiat. Res., 52, 69–74 (2011) Regular Paper

Multi-institutional Retrospective Analysis of the Inhomogeneity Correction for Radiation Therapy of Lung Cancer

Hideyuki MIZUNO[1]*, Hiroyuki OKAMOTO[2], Miyoko FUKUOKA[3], Yuji HANYU[3], Masahiko KUROOKA[4], Ryosuke KOHNO[5], Teiji NISHIO[5], Yu KUMAZAKI[6], Hidenobu TACHIBANA[7], Yutaka TAKAHASHI[8], Shinichiro MORI[1], Norihisa MASAI[9] and Koji SASAKI[10]

Inhomogeneity correction/Retrospective analysis/Treatment planning/QA/TPS.

The purpose of this work is to retrospectively analyze the effect of the inhomogeneity correction using clinically treated plan of stage III non-small-cell lung cancer within multiple institutions in Japan. Twenty-five patients among five facilities of radiation therapy were registered for this study. The isocenter dose or D_{95} of PTV or other important values were compared with and without an inhomogeneity correction using model-based algorithm. The differences in isocenter dose were 4% average and 10% maximum for the first Anterior-Posterior opposed field plan to 40 Gy and 6% average and 11% maximum for the off-cord boost oblique field plan of 20 Gy. The differences in D_{95} dose were 1% average and 9% maximum for the first plan and 1% average and 6% maximum for the boost plan. D_{95} prescription seemed to be a superior method; however, its reliability depends on each clinical case. Additionally, maximum dose, minimum dose and mean dose for both the primary tumor and the metastatic lymph node were analyzed, and the minimum dose had the most impressive results. In some cases, the target volume had unintended underdose of more than 10%. Finally, an analysis of the organ at risk was added, and this showed no meaningful differences for the V_{20} of the lung and the maximum dose of the spinal cord. These results provide a standard for the effects of the inhomogeneity correction.

INTRODUCTION

The influence of the inhomogeneity correction in treatment planning for radiation therapy is important, especially for lung cancer.[1–5] The RTOG-8808 study found that the mean inhomogeneity correction factor at the isocenter (IC) for 322 patients was 1.05 ± 0.05 (standard deviation) with an overall range of 0.95–1.28.[6] This study was limited to a single central plane planning and the one-dimensional (1-D) correction method was used (*e.g.*, the Batho correction method). Recently, model-based algorithms have become available in commercial treatment planning systems. As model-based algorithms consider 3-D inhomogeneity corrections through kernel deformation, the precision of the inhomogeneity correction is greatly improved. Obviously the effect of the inhomogeneity correction also differs from past studies that used the 1-D correction method. Hasenbalg *et al.*[7] studied the comparison study between convolution superposition algorithm and anisotropic analytic algorithm (AAA) with a Monte Carlo program (VMC++). They found dose discrepancies between the algorithms and VMC++ for the median value of the PTV of typically 0.4% (range: 0.0 to 1.4%) in the lung and −1.3% (range: −2.1 to −0.6%) in the breast for the few cases they analyzed. Some studies have reported differences using a model-base algorithm for stereotactic radiotherapy.[8–10] Those studies indicated that the variation in the differences depends on the location of the tumor as well as on beam geometry. Also, there may be a dependence to the local facility policy of radiation oncologists or medical physicists of treatment planning. The pur-

*Corresponding author: Phone: +81(43)206-3178,
Fax: +81(43)206-3246,
E-mail: h_mizuno@nirs.go.jp

[1]Research Center for Charged Particle Therapy, National Institute of Radiological Sciences, Anagawa 4-9-1, Inage, Chiba 263-8555, Japan; [2]Radiation Oncology Divisions, National Cancer Center Hospital; [3]Department of Radiation Oncology, Tokyo Women's Medical University Hospital; [4]Kanagawa Cancer Center; [5]Particle Therapy Division, Research Center for Innovative Oncology, National Cancer Center Hospital East; [6]Department of Radiation Oncology, Saitama Medical University International Medical Center; [7]Department of Radiation Oncology, The Cancer Institute Hospital of JFCR; [8]Department of Radiation Oncology, Osaka University Graduate School of Medicine; [9]Miyakojima IGRT Clinic; [10]Department of Radiological Technology, Gunma Prefectural Graduate School of Health Sciences.

doi:10.1269/jrr.10066

pose of this work is to retrospectively analyze the effect of the inhomogeneity correction using clinically treated cases within multiple institutions in Japan. The IC dose or D_{95} of PTV or other important values was compared with and without the inhomogeneity correction. These results will provide a basis for the effects of the inhomogeneity correction and should be useful for those institutions preparing to adopt an inhomogeneity correction as well as those institutions already using a model-based algorithm but have not carefully considered the effects of the inhomogeneity correction.

MATERIALS AND METHODS

We chose stage III non-small cell lung cancer, which reportedly has a high inhomogeneity correction factor. According to the treatment planning guidelines published by the Japanese Society for Therapeutic Radiology and Oncology (JASTRO),[11] cases are treated in two steps. The first step is irradiation to the primary tumor (PTVp), metastatic lymph node (PTVn), and the preventive region, using anterior–posterior (AP) opposed fields for 40 Gy. The second step is the off-cord boost step to the PTVp and PTVn using only oblique opposed fields for 20 Gy.

The retrospective study was applied to the clinically treated cases in which the inhomogeneity correction was not considered. We recalculated the plans using the inhomogeneity correction "On" with a model-based algorithm, while the monitor units (MU) were equal to the original (treated) value. If we assume that the calculated results using a model-based algorithm were almost accurate, we can estimate the actual delivered dose by this retrospective study. The main parameters that we analyzed were the IC dose and the D_{95} of PTV2 (defined by PTVp + PTVn). These are critical parameters for dose prescription. Furthermore, maximum dose, minimum dose, averaged dose, and D_{95} for each target (PTVp and PTVn) were analyzed. Five facilities participated in this study with each facility having five cases. Standard planning information such as treatment planning system (TPS), the name of model based algorithm used, X-ray energy and MLC margin for each institution are listed in Table 1. Tumor (position and size) and beam (field size and depth) information for each case are listed in Table 2.

Table 1. Standard planning information of each institution

Institution	TPS	Model based algorithm	X-ray energy	MLC margin
A	XiO	Superposition	10 MV	10 mm
B	XiO	Superposition	6 MV	5 mm
C	XiO	Superposition	6–15 MV	5 mm
D	Eclipse	AAA	6 MV	5 mm
E	XiO	Superposition	10 MV	5 or 8 mm

RESULTS

IC dose and D_{95} of PTV2

The results of IC dose differences and D_{95} differences of PTV2 between inhomogeneity corrected (On) and uncorrected (Off) conditions are shown in Fig. 1a and 1b. Figure

Table 2. Tumor (position and size) and beam (field size and depth) information of each case studies

Institution	Case number	Tumor location	PTVp [cm^3]	PTVn [cm^3]	Field size [cm^2]	Depth/ Effective depth
A	1	LUL	32	118	11.2 × 14.4	9.1/6.9 cm
	2	LUL	80	125	15.8 × 13.0	9.9/4.4 cm
	3	RLL	16	27	15.3 × 11.0	10.2/7.0 cm
	4	RUL	28	66	9.2 × 11.2	9.9/3.2 cm
	5	RUL	19	147	15.5 × 12.5	9.8/5.4 cm
B	6	LUL	58	15	11.9 × 9.2	8.5/6.4 cm
	7	RLL	101	45	16.8 × 18.8	8.9/4.9 cm
	8	RUL	95	235	10.8 × 14.4	9.1/9.2 cm
	9	LUL	215	183	15.4 × 10.5	7.5/6.4 cm
	10	LUL	368	151	15.1 × 10.3	8.4/6.1 cm
C	11	LUL	45	18	11.7 × 10.8	8.6/8.9 cm
	12	RUL	338	36	13.3 × 13.1	8.8/8.3 cm
	13	LUL	161	269	11.5 × 17.6	10.5/10.5 cm
	14	RML	254	14	12.9 × 10.1	10.8/4.9 cm
	15	LLL	153	138	11.4 × 16.4	12.1/11.6 cm
D	16	LUL	277	60	12.7 × 11.4	7.1/6.1 cm
	17	RUL	68	165	11.1 × 14.4	5.1/5.2 cm
	18	LUL	122	127	11.9 × 17.9	8.7/8.0 cm
	19	LUL	162	315	15.4 × 16.4	6.3/6.5 cm
	20	LUL	212	201	16.5 × 17.4	12.1/11.9 cm
E	21	RML	63	85	12.1 × 13.6	12.6/5.8 cm
	22	RML	136	57	10.1 × 14.4	9.2/8.1 cm
	23	RML	157	34	8.3 × 7.0	11.9/11.4 cm
	24	RUL	178	54	10.5 × 10.0	13.6/6.7 cm
	25	RML	112	35	15.7 × 15.9	11.1/11.1 cm

*Abbreviations: PTVp, planning target volume of primary tumor; PTVn, planning target volume of metastatic lymph node; LLL, left lower lobe; LUL, left upper lobe; RLL, right lower lobe; RML, right middle lobe; RUL = right upper lobe.

*Institution "D" has completed the adoption of the inhomogeneity correction using a model-based algorithm and has a clinical plan that was also completed with corrected condition. We included these data because we expected that their effect on comparing relative parameters was not significant.

*Field sizes and depths correspond to the anterior (gantry 0 degree) beam of AP fields.

1a shows the data of the first AP opposed fields of 40 Gy, and Fig. 1b shows the data of oblique opposed fields of off-cord boost irradiation of 20 Gy. The differences in the IC dose were 4% average and 10% (Case 21) maximum for the first plan (1a) and 6% average and 11% (Case 20) maximum for the boost plan (1b). The differences in the D_{95} dose were 1% average and 9% (Case 4) maximum for the first plan (1a) and 1% average and 6% (Case 8) maximum for the boost plan (1b).

D_{95}, Dmax, Dmin, and Dmean of PTVp

D_{95}, maximum dose (Dmax), minimum dose (Dmin), and

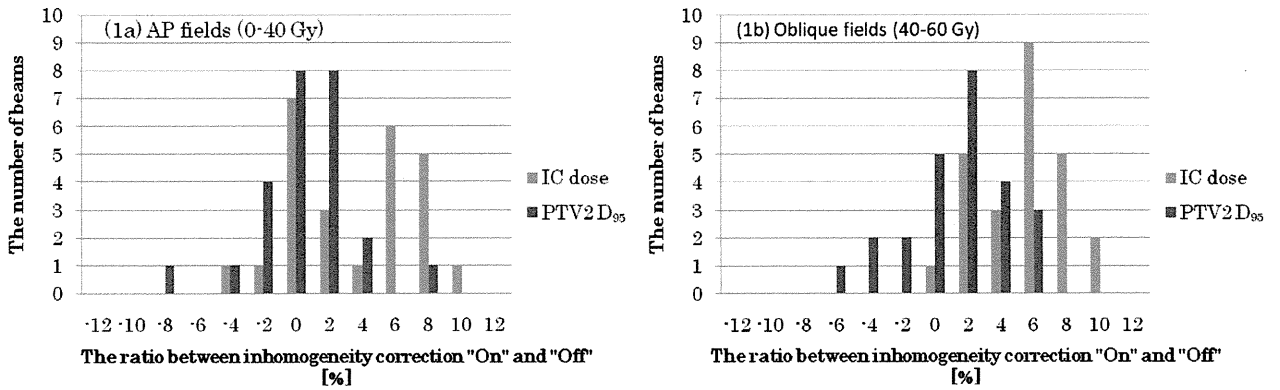

Fig. 1. The ratio between inhomogeneity correction "On" and "Off" of the isocenter (IC) dose and PTV2 D_{95} for the first plan (AP opposed fields; 0–40 Gy) (1a) and the off-cord boost plan (oblique fields; 40–60 Gy) (1b).

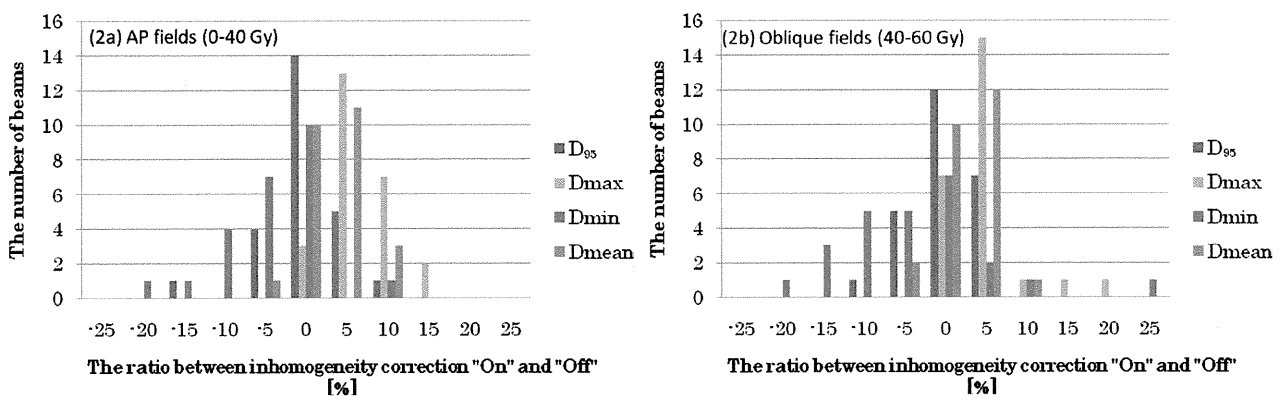

Fig. 2. The ratio between inhomogeneity correction "On" and "Off" of the D_{95}, Dmax, Dmin, and Dmean of PTVp for the first plan (AP opposed fields; 0–40 Gy) (2a) and the off-cord boost plan (oblique fields; 40–60 Gy) (2b).

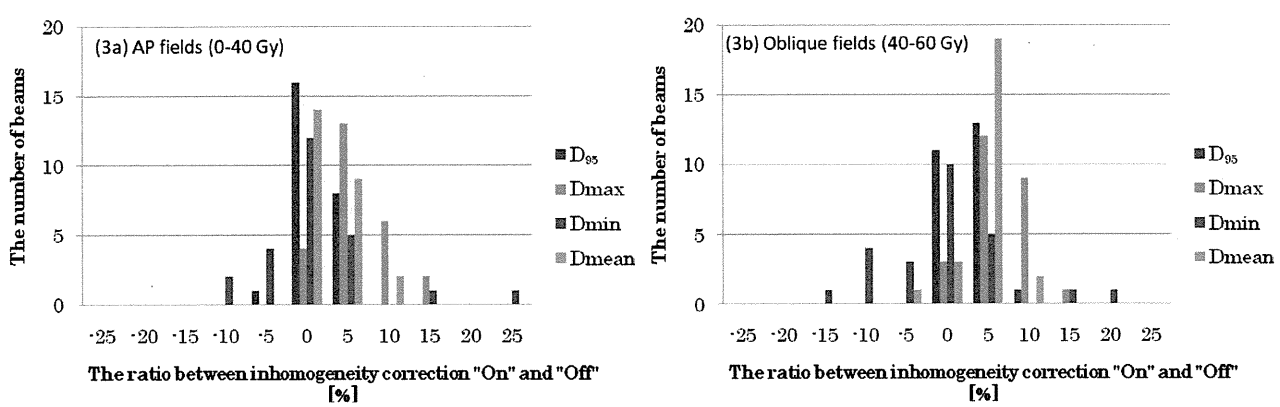

Fig. 3. The ratio between inhomogeneity correction "On" and "Off" of the D_{95}, Dmax, Dmin, and Dmean of PTVn for the first plan (AP opposed fields; 0–40 Gy) (3a) and the off-cord boost plan (oblique fields; 40–60 Gy) (3b).

Table 3. Differences between corrected and uncorrected conditions for the V_{20} [%] of the lung and the Dmax [Gy] of spinal cord

Case	V_{20} [%] of lung			Dmax [Gy] of spinal cord		
	Uncorrected (A)	Corrected (model-based) (B)	Differences (B)–(A)	Uncorrected (C)	Corrected (model-based) (D)	Differences (D)–(C)
1	21.1	21.6	+0.5	46.3	45.7	–0.7
2	25.7	26.1	+0.4	46.0	47.2	+1.2
3	27.4	28.2	+0.8	47.8	48.2	+0.4
4	17.5	18.4	+0.9	36.4	38.0	+1.7
5	34.7	35.6	+0.9	44.0	44.3	+0.3
6	15.1	15.5	+0.4	45.8	45.1	–0.7
7	36.4	37.3	+0.9	48.8	49.5	+0.7
8	30.8	31.6	+0.8	52.9	53.2	+0.3
9	29.0	29.4	+0.4	49.6	49.5	0.0
10	27.0	27.5	+0.5	48.2	49.2	+1.1
11	23.2	23.6	+0.4	41.8	41.8	0.0
12	16.6	17.1	+0.5	45.9	45.8	–0.1
13	30.9	30.2	–0.7	47.9	48.1	+0.2
14	29.1	30.3	+1.2	44.9	45.7	+0.9
15	17.0	17.4	+0.4	42.4	42.6	+0.2
16	23.9	25.2	+1.3	42.4	42.7	+0.3
17	12.2	12.3	+0.1	46.8	47.4	+0.6
18	27.9	29.4	+1.5	41.9	41.6	–0.3
19	21.7	22.6	+0.9	46.5	45.6	–0.9
20	29.3	30.4	+1.1	47.0	46.3	–0.7
21	33.1	34.6	+1.5	44.2	44.6	+0.4
22	17.1	17.4	+0.3	44.5	47.5	+3.1
23	15.2	15.4	+0.2	45.5	45.9	+0.4
24	15.9	16.5	+0.6	47.6	49.2	+1.6
25	37.3	39.8	+2.5	43.9	46.2	+2.3

mean dose (Dmean) were calculated for PTVp. The results are shown in Fig. 2a and 2b. Figure 2a shows the data of the first AP opposed fields of 40 Gy, and Fig. 2b shows the data of oblique opposed fields of off-cord boost irradiation of 20 Gy.

D_{95}, Dmax, Dmin, and Dmean of PTVn

We analyzed similar data for the PTVn. D_{95}, Dmax, Dmin, and Dmean were calculated for the PTVn. Figure 3a shows the data of first AP opposed fields of 40 Gy and Fig. 3b shows the data of oblique opposed fields of off-cord boost irradiation of 20 Gy.

V_{20} of lung and Dmax of spinal cord

A slight increase in the V_{20} of the lung could be seen; however, there was no notable difference between uncorrected and corrected conditions (Table 3).

DISCUSSION

From the analysis of the IC dose, systematical overdose was delivered to the IC. If we apply the inhomogeneity correction without any consideration regarding the way of dose prescription, about 5% underdosage on average may occur with an IC dose. The main reason that an underdosage occur is considered to be a decrease in the effective depth of the beam path within the lung region because of low density. For the first plan of Case 21 (10% underdosage), differences between the physical depth and the effective depth were 12.6 cm and 5.8 cm, respectively, for the anterior beam and 7.3 cm and 5.1 cm, respectively, for the posterior beam. For the boost plan of Case 20 (11% underdosage), these values